



Large-eddy simulation of offshore wind farm

Di Yang, Charles Meneveau, and Lian Shen

Citation: [Physics of Fluids \(1994-present\)](#) **26**, 025101 (2014); doi: 10.1063/1.4863096

View online: <http://dx.doi.org/10.1063/1.4863096>

View Table of Contents: <http://scitation.aip.org/content/aip/journal/pof2/26/2?ver=pdfcov>

Published by the [AIP Publishing](#)



Re-register for Table of Content Alerts

Create a profile.



Sign up today!



Large-eddy simulation of offshore wind farm

Di Yang,^{1,2} Charles Meneveau,^{1,2} and Lian Shen^{3,4, a)}

¹*Department of Mechanical Engineering, Johns Hopkins University, Baltimore, Maryland 21218, USA*

²*Center for Environmental and Applied Fluid Mechanics, Johns Hopkins University, Baltimore, Maryland 21218, USA*

³*Department of Mechanical Engineering, University of Minnesota, Minneapolis, Minnesota 55455, USA*

⁴*St. Anthony Falls Laboratory, University of Minnesota, Minneapolis, Minnesota 55414, USA*

(Received 27 June 2013; accepted 16 December 2013; published online 4 February 2014)

A hybrid numerical capability is developed for the simulation of offshore wind farms, in which large-eddy simulation is performed for the wind turbulence, and a potential flow based method is used for the simulation of the ocean wave field. The wind and wave simulations are dynamically coupled. The effect of wind turbines on the wind field is represented by an actuator disk model. This study focuses on the effect of wind-seas, and the turbine motion is treated as negligibly small. A variety of fully-developed and fetch-limited wind-sea conditions and turbine spacings are considered in the study. Statistical analyses are performed for the simulation results, with a focus on the mean wind profile, kinetic energy budget in the wind field, and the wind turbine power extraction rate. The results indicate that the waves have appreciable effect on the wind farm performance. The wind turbines obtain a higher wind power extraction rate under the fully developed wind-sea condition compared with that under the fetch-limited condition. This higher extraction rate is caused by the faster propagating waves and the lower sea-surface resistance on the wind when the wind-seas are fully developed. The wave-induced difference can be as high as 8% with the commonly used turbine spacing in commercial land-based wind farms, $s_x = 7$ (with s_x being the ratio of streamwise turbine spacing to the turbine diameter). Such level of difference is noteworthy considering the previous understanding that direct wave-induced disturbance to the wind field decays exponentially away from wave surface. © 2014 AIP Publishing LLC. [<http://dx.doi.org/10.1063/1.4863096>]

I. INTRODUCTION

Being renewable and not having major adverse environmental and climate impacts, wind power plays an increasingly important role in energy. Over the past several decades, many experiments, theoretical analyses, and numerical simulations have been conducted to improve our understanding of wind turbine dynamics for design purposes. The aerodynamics and wake structure of a single wind turbine have been explored extensively.^{1–4} In particular, recent advancement in large-eddy simulation (LES) combined with wind turbine models has made LES a useful tool for wind energy research.^{5–7} LES of a single wind turbine in turbulence shear flows⁸ showed good agreement with wind-tunnel measurement data.⁹

Meanwhile, the size of modern commercial wind farms has evolved into considerably large scales, with the number of turbines being $O(100–1000)$ and the length of the turbine blades being $O(50\text{ m})$ or longer. With such sizes, the flows past the wind farms approach the regime of fully developed turbulent boundary layers, and there are substantial interactions among the turbulent

^{a)} Author to whom correspondence should be addressed. Electronic mail: shen@umn.edu.

wakes of wind turbines and the atmospheric boundary layer.^{10–12} By performing LES of a wind turbine array with periodic lateral boundary conditions, Calaf *et al.*¹¹ were able to capture the complex interaction of wind turbine wakes, as well as the large-scale interaction between the wind farm and the atmospheric boundary layer. Particularly, their statistical analyses of the LES results revealed that for a fully developed wind turbine array boundary layer, the wind at the turbine rotor height obtains kinetic energy mainly through the vertical flux of energy from the atmosphere above, rather than from the horizontal energy flux. This mechanism is also supported by the wind-tunnel measurement of Cal *et al.*¹³ and further more recent LES studies.¹⁴ With the vertical supplement of kinetic energy into the wind farm, the inflow velocity for the wind turbines inside the large wind farm remains statistically steady with sufficient magnitude,¹⁵ enabling the entire wind farm to continuously extract wind power from the atmosphere.

While wind power on land is being actively explored, there is also a consensus that offshore wind power will be the next research frontier. For energy harvesting, winds over water have many advantages over winds on land. For example, large sea areas, where the wind turbines will be invisible from the coastal line if installed more than 20 miles offshore, are available for wind farm deployment. Offshore winds are usually stronger than winds on land. As a result, larger wind turbines can be installed at relatively lower heights offshore. On the other hand, the presence of ocean waves also introduces complexities to the operation of wind turbines.¹⁶ The dynamical coupling between wind and waves makes offshore winds significantly more difficult to characterize than winds over land.^{17,18} Therefore, there is a critical need to study marine winds for energy applications.

Unlike for many land-based wind farms, offshore wind farms are usually located in wide open areas. The sea surface is covered by wind-generated waves with broadband spectra. Such condition poses a challenge on wind-tunnel measurement. Meanwhile, although many field measurements have yielded valuable data for wind–wave interaction studies,^{19,20} such measurements in offshore wind farms have not yet been systematically conducted to date. These technical difficulties make numerical simulation a good alternative research tool at the current stage.

In the past decade, LES has been applied to study wind–wave interaction.^{21–23} Recently, Yang and Shen^{24,25} have developed a numerical capability for the simulation of turbulence–wave interaction in generalized wave-following coordinates. It has been applied to study the interaction of wind turbulence with broadband ocean waves.²⁶

In the present study, we extend the coupled wind–wave simulation tool of Refs. 25 and 26 to the simulation of a fully developed offshore wind farm boundary layer. The effect of wind turbine rotors on the atmospheric flow is modeled using an actuator-disk model,^{5,6} which has recently been applied to the study of land-based wind farms.^{11,27} In order to accurately model the wind turbulence inside the wind farms as well as near the sea surface, a scale-dependent dynamic Smagorinsky model with Lagrangian averaging²⁸ is employed and fitted into the current wave-following coordinate system. The performance of the current LES code is tested by the simulations of wind turbulence past both a single wind turbine and a wind turbine array boundary layer.

In this study, we perform a series of simulations to study the dynamics of the marine atmospheric boundary layer and its interaction with the embedded offshore wind farm. We focus on the effect of wind-seas on the wind farm. Effect of swells, which are generated by storms far away and propagate to the wind farm location in the form of long crested, large amplitude, long waves, is beyond the scope of this paper and will be a subject of our follow-up study. Consistent with the present focus on the wind-seas not the swells, the wind turbine platforms are treated as stationary in our simulations, because floating wind turbine platforms from many designs, e.g., the MIT/NREL TLP²⁹ and the WindFloat,³⁰ have very small motions in response to the wind-seas.

For the wind-seas, we consider both fetch-limited³¹ and fully developed³² conditions. At these different stages of wave development, the wave field possesses different phase speeds at the peak of the spectrum, and thus imposes different sea-surface drag on the wind. For each wave condition, we further consider three different values of the streamwise wind turbine spacing. Statistical analyses are performed for the simulation results to investigate the effect of the wave motions and turbine spacing on the wind farm, with a focus on time- and horizontal-averaged flow statistics including mean velocity profiles and kinetic energy budgets. The performance of the wind farm is also studied

by the direct calculation of power extraction rate based on the wind force and velocity at the turbine disk.

This paper is organized as follows. In Sec. II, the hybrid simulation method for offshore wind farm is described. In Sec. III, the numerical method is tested and validated. In Sec. IV, the dynamics of offshore wind farm is studied. In particular, the cases considered and the parameters for the simulations are introduced in Sec. IV A, and the results are presented in Secs. IV B–IV E. Finally, conclusions are given in Sec. V.

II. NUMERICAL METHOD FOR WIND AND WAVE SIMULATIONS AND MODELING OF WIND TURBINES

A. Large-eddy simulation of wind turbulence

For the wind field, we consider a neutrally stratified atmospheric boundary layer flow in a horizontally periodic domain. The coordinate system is denoted as $x_i (i = 1, 2, 3) = (x, y, z)$, where x and y are the horizontal coordinates and z is the vertical coordinate, with $z = 0$ being the mean water level. The velocity components in x -, y -, and z -directions are denoted as $u_i (i = 1, 2, 3) = (u, v, w)$, respectively.

In LES, the motion of wind turbulence is described by the filtered incompressible Navier–Stokes equations

$$\frac{\partial \tilde{u}_i}{\partial t} + \tilde{u}_j \frac{\partial \tilde{u}_i}{\partial x_j} = -\frac{1}{\rho_a} \frac{\partial \tilde{p}^*}{\partial x_i} - \frac{\partial \tau_{ij}^d}{\partial x_j} - \frac{1}{\rho_a} \frac{\partial p_\infty}{\partial x} \delta_{i1} + f_T \delta_{i1}, \quad (1)$$

$$\frac{\partial \tilde{u}_i}{\partial x_i} = 0. \quad (2)$$

Here, $(\tilde{\dots})$ indicates filtering at the grid scale Δ ; ρ_a is the density of air; $\tau_{ij} = \widetilde{u_i u_j} - \tilde{u}_i \tilde{u}_j$ is the subgrid-scale (SGS) stress tensor, and τ_{ij}^d is its trace-free part; and $\tilde{p}^* = \tilde{p} + \tau_{kk}/3 - p_\infty$ is the filtered modified pressure. In this study, we consider the condition of mean wind being perpendicular to the wind turbine rotor plane, i.e., along the $+x$ -direction. The imposed pressure gradient $\partial p_\infty / \partial x$ models the effect of geostrophic wind forcing (see the discussion in Ref. 11). The friction velocity for the wind above the turbine array is thus

$$u_* = \sqrt{-\frac{\overline{H}}{\rho_a} \frac{\partial p_\infty}{\partial x}}, \quad (3)$$

where \overline{H} is the mean height of the computational domain.

The turbine-induced force in Eq. (1), f_T , is calculated by the actuator-disk model originally applied in LES by Jimenez *et al.*^{5,6} In the present study, we use the modified version proposed by Meyers and Meneveau,³³ in which the averaged velocity at the turbine rotor disk is used as the reference velocity, rather than the upstream undisturbed wind velocity originally used in Jimenez *et al.*^{5,6} Such modification has been shown to be necessary for wind turbine array boundary layer flow, since most of the turbines sit within the wakes of the preceding turbines.¹¹ In the model, the turbine induced force per unit mass in the streamwise direction is given by

$$f_T(x_i, y_j, z_k) = -\frac{1}{2} C'_T \langle u^T \rangle_d^2 \frac{\gamma_{j,k}}{\Delta x}. \quad (4)$$

Here, (x_i, y_j, z_k) denotes the position of a given grid point with index (i, j, k) ; $C'_T = C_T / (1 - a)^2$ is the effective thrust coefficient,¹¹ where C_T is the turbine thrust coefficient for undisturbed wind velocity and a is the induction factor;³ $\langle u^T \rangle_d$ is the local reference wind velocity evaluated by spatial averaging over all grid points within the turbine disk; $\gamma_{j,k}$ is the fraction of area overlap between the grid cell (j, k) and the turbine rotor circle; and Δx is the streamwise grid size. We note that Calaf *et al.*¹¹ used a different reference velocity $\langle \overline{u}^T \rangle_d$, in which an additional temporal averaging is performed over a time window. In the present study, we use $\langle u^T \rangle_d$ without temporal averaging to capture the short-term variability of f_T induced by the wave passage.

In this study, we use a typical value $C_T = 3/4$ for the thrust coefficient, which holds for a hub-height incoming wind speed of 7–11 m/s.⁵ We use a value of $a = 1/4$ for the induction factor. This gives $C'_T = 4/3$. The same values for C_T and a have also been used in several previous LES.^{11,14,33,34} Moreover, Meyers and Meneveau³³ showed that $C'_T = [4a/(1-a)][1 + (C_D/C_L)(2/\lambda)]$, where C_D and C_L are the lift and drag coefficients of the turbine blade, respectively, and λ is the tip-speed ratio. In practice, a fixed value for C'_T may be obtained through pitch control. So for clarity of analysis and discussion, in this study we use the fixed value of $C'_T = 4/3$ for all the wind farm simulations.

In Eq. (1), the SGS stress tensor is modeled using the Lagrangian-averaged scale-dependent (LASD) dynamic Smagorinsky model, as described in Ref. 28. It was shown that the Lagrangian averaging scheme along the fluid pathline provides accurate turbulence statistics yet preserves local variability and Galilean invariance;³⁵ and the scale-dependent approach provides more accurate predictions of turbulence in the near-surface region.³⁶ These features make the LASD model an appropriate choice for the LES of canopy-like wind turbine array boundary layer turbulence over complex sea-surface waves.

In Eq. (1), the molecular viscous term is neglected because the Reynolds number for the flows considered in this study is very high; it also prevents resolving of the turbulence boundary layer near the wave surface. Consequently, in the simulation, a surface-layer model based on law-of-the-wall is employed to impose proper sea-surface stress to the wind turbulence, which is expressed as^{23,28,37}

$$\tau_{xz}^{SGS}(x, y, t) = -C_d \widehat{U}_r(x, y, t) (\widehat{u}_r(x, y, t)e_x^\parallel + \widehat{w}_r(x, y, t)e_x^\perp), \quad (5)$$

$$\tau_{yz}^{SGS}(x, y, t) = -C_d \widehat{U}_r(x, y, t) (\widehat{v}_r(x, y, t)e_y^\parallel + \widehat{w}_r(x, y, t)e_y^\perp), \quad (6)$$

with

$$C_d = \left[\frac{\kappa}{\ln(d_2/z_0)} \right]^2 \quad (7)$$

being the drag coefficient given by the logarithmic law and d_2 being the vertical distance of the first off-surface grid-point to the sea surface. Here,

$$(e_x^\parallel, 0, e_x^\perp) = \left(\frac{1}{\sqrt{1 + (\partial\widehat{\eta}/\partial x)^2}}, 0, \frac{\partial\widehat{\eta}/\partial x}{\sqrt{1 + (\partial\widehat{\eta}/\partial x)^2}} \right) \quad (8)$$

and

$$(0, e_y^\parallel, e_y^\perp) = \left(0, \frac{1}{\sqrt{1 + (\partial\widehat{\eta}/\partial y)^2}}, \frac{\partial\widehat{\eta}/\partial y}{\sqrt{1 + (\partial\widehat{\eta}/\partial y)^2}} \right) \quad (9)$$

are the unit vectors tangential to the wave surface in the (x, z) - and (y, z) -planes, respectively; $\widehat{\eta}(x, y, t)$ is the filtered instantaneous wave surface elevation; $\kappa = 0.4$ is the von Kármán constant; $(\widehat{\dots})$ indicates filtering at the test-filter scale 2Δ ; z_0 is the sea-surface roughness associated with the SGS waves; $(\widehat{u}_r, \widehat{v}_r, \widehat{w}_r)$ are the filtered wind velocities relative to the water surface at the first off-surface grid-point (i.e., in the LES code, at height d_2 above the sea surface),

$$\widehat{u}_{r,i}(x, y, t) = \widehat{u}_i(x, y, d_2, t) - \widehat{u}_{s,i}(x, y, t), \quad i = 1, 2, 3. \quad (10)$$

Here, the values of $\widehat{u}_{s,i}$ are obtained by the test-filtering of the sea surface velocities $u_{s,i}$, which are given in Sec. II B [see Eqs. (16)–(18)]; and

$$\widehat{U}_r(x, y, t) = \sqrt{\left[\widehat{u}_r(x, y, t)e_x^\parallel + \widehat{w}_r(x, y, t)e_x^\perp \right]^2 + \left[\widehat{v}_r(x, y, t)e_y^\parallel + \widehat{w}_r(x, y, t)e_y^\perp \right]^2} \quad (11)$$

is the magnitude of tangential wind velocity relative to the wave surface.

We note that the logarithmic similarity law-of-the-wall was originally obtained in an averaged sense. To apply it locally, in Eqs. (5) and (6) we have used the test-filtered velocities at the scale 2Δ , $(\widehat{u}_r, \widehat{v}_r, \widehat{w}_r)$, instead of the grid-resolved velocities, $(\widetilde{u}_r, \widetilde{v}_r, \widetilde{w}_r)$. This filtering treatment reduces velocity fluctuations significantly and thus improves the applicability of Eqs. (5) and (6) (for detailed discussions see Ref. 28).

In the simulations, the streamwise and spanwise boundaries are treated as periodic, so that the finite number of wind turbines in the simulation domain represent a subset of an infinitely large wind farm.¹¹ The top of the simulation domain is considered to be rigid and free-slip. The bottom is bounded by the surface of water waves, with von Neumann condition for the velocity field given by Eqs. (5) and (6). A detailed discussion of the surface wave parameters and the sea-surface roughness z_0 is given in Sec. IV A. A time-dependent boundary-fitted grid is used to follow the curvature of the wave surface. The irregular wave surface-bounded domain in the physical space (x, y, z, t) is transformed to a right rectangular prism in the computational space (ξ, ψ, ζ, τ) with the following algebraic mapping:

$$\tau = t, \quad \xi = x, \quad \psi = y, \quad \zeta = \frac{z - \tilde{\eta}(x, y, t)}{\tilde{H}(x, y, t)} = \frac{z - \tilde{\eta}(x, y, t)}{\bar{H} - \tilde{\eta}(x, y, t)}. \quad (12)$$

Here, the height of the physical domain, $\tilde{H}(x, y, t)$, is decomposed into the average height \bar{H} and the wave induced variation $-\tilde{\eta}(x, y, t)$.

For spatial discretization in the computational space (ξ, ψ, ζ, τ) , we use a Fourier-series-based pseudo-spectral method on a collocated grid in the horizontal directions, and a second-order finite-difference method on a staggered grid in the vertical direction. The governing equations are integrated in time with a fractional-step method. First, the momentum equations without the pressure terms are advanced in time with a second-order Adams–Bashforth scheme. Then, a Poisson equation is solved for the pressure to provide correction for the velocity field so that the incompressibility constraint is satisfied. The effect of resolved-scale sea-surface waves on the wind field, i.e., the form drag, is captured by this wave-correlated pressure field. The details and validation of the numerical scheme are provided in Ref. 24.

B. High-order simulation of sea-surface waves

The motion of the sea-surface waves is simulated using a high-order spectral method (HOSM).³⁸ The HOSM simulates nonlinear waves using the Zakharov formulation,³⁹ in which the wave motion is described by the surface elevation η and the surface potential Φ^s . Here, $\Phi^s = \Phi(x, y, z = \eta(x, y, t), t)$ with Φ being the velocity potential. The wave motion is governed by the kinematic and dynamic conditions at the sea surface $z = \eta(x, y, t)$,

$$\frac{\partial \eta}{\partial t} + \nabla_h \eta \cdot \nabla_h \Phi^s - (1 + \nabla_h \eta \cdot \nabla_h \eta) \frac{\partial \Phi}{\partial z} = 0, \quad (13)$$

$$\frac{\partial \Phi^s}{\partial t} + g\eta + \frac{1}{2} \nabla_h \Phi^s \cdot \nabla_h \Phi^s + \frac{p_a}{\rho_w} - \frac{1}{2} (1 + \nabla_h \eta \cdot \nabla_h \eta) \left(\frac{\partial \Phi}{\partial z} \right)^2 = 0, \quad (14)$$

and the incompressibility constraint over the body of water described by the Laplace equation

$$\nabla^2 \Phi = \frac{\partial^2 \Phi}{\partial x^2} + \frac{\partial^2 \Phi}{\partial y^2} + \frac{\partial^2 \Phi}{\partial z^2} = 0. \quad (15)$$

In Eqs. (13) and (14), $\nabla_h = (\partial/\partial x, \partial/\partial y)$ is the horizontal gradient; g is the gravitational acceleration; p_a is the air pressure at the wave surface; ρ_w is the density of water; and the operator ‘ \cdot ’ denotes the dot product of two vectors. In HOSM, Eqs. (13) and (14) are discretized in space by a triple-perturbation method, with a Taylor expansion about the mean water surface in the vertical direction and Fourier-series-based pseudo-spectral method in the horizontal directions. Details of the HOSM are given in Appendix A.

At each timestep, the values of $\eta(x, y, t)$, $\Phi^s(x, y, t)$ and $\Phi(x, y, z, t)$ are calculated. The wave orbital velocities at the sea surface are obtained as³⁸

$$u_s(x, y, t) = \frac{\partial \Phi^s}{\partial x} - \frac{\partial \eta}{\partial x} \frac{\partial \Phi}{\partial z} \Big|_{z=\eta}, \quad (16)$$

$$v_s(x, y, t) = \frac{\partial \Phi^s}{\partial y} - \frac{\partial \eta}{\partial y} \frac{\partial \Phi}{\partial z} \Big|_{z=\eta}, \quad (17)$$

$$w_s(x, y, t) = \frac{\partial \Phi}{\partial z} \Big|_{z=\eta}. \quad (18)$$

The HOSM simulation of sea-surface wave field is coupled with the LES of wind turbulence through a fractional-step scheme as described in Ref. 25. At each timestep of the wind and wave simulations, first the HOSM simulation advances the wave field in time with the wind pressure forcing obtained from the wind LES of the previous timestep, and provides the updated sea-surface elevation η and velocity \mathbf{u}_s to the wind LES. In particular, in the HOSM we use higher horizontal resolution than the wind LES, so that all of the energy-containing waves in the wave spectrum are resolved. This higher-resolution treatment for HOSM is enabled by its much lower computational cost compared with the LES. Then the wind LES uses the grid-filtered $\tilde{\eta}$ and $\tilde{\mathbf{u}}_s$ for the surface-layer modeling in Eqs. (5) and (6) and for the grid mapping in Eq. (12). The LES thus advances the wind field in time for a timestep. As a result, the entire wind and wave fields advance to the next timestep, and the above calculations repeat.

III. TEST AND VALIDATION

The current turbulence flow solver has been tested extensively for various wind-wave problems.^{24,25,40,41} Therefore, the validation of wind-wave interaction simulation is not taken up in this paper. Here, we focus on the validation of wind turbine modeling by comparing the current LES result with existing measurement and simulation data in the literature.

A. Simulation of single wind turbine in turbulent flow

First, we perform LES of air flow past a single wind turbine over solid surface, with the parameters matching those in the laboratory measurement of Chamorro and Porté-Agel.⁹ The wind turbine has a diameter of $D = 0.15$ m and a hub height of $H_{\text{hub}} = 0.125$ m. The mean inflow velocity (measured at $1D$ upstream of wind turbine hub) is $U_{\text{hub}} = 2.2$ m/s. The wind friction velocity is $u_* = 0.102$ m/s. The bottom boundary is flat and has a surface roughness specified as $z_0 = 0.03$ mm.

The simulation domain has a size of $(L_x, L_y, \overline{H}) = (4.32, 0.72, 0.46)$ m. The domain is sufficiently long in the streamwise direction ($L_x/D = 28.8$), so that the effect of periodic boundary condition on the statistics of the inflow wind towards the turbine rotor is negligibly small. The domain height matches the measured boundary-layer depth from the experiments. The use of a rigid and free-slip top boundary condition is a reasonable configuration for the simulation to mimic the experimental condition.⁸ The grid resolution is $N_x \times N_y \times N_z = 256 \times 48 \times 64$, with evenly distributed grid points in all of the three directions. The flow initially has a logarithmic mean velocity profile with randomly seeded fluctuations. The flow field is advanced in time with a timestep of 1.0×10^{-3} s till the wind turbulence in the turbine wake reaches a statistically steady state. The simulation is then continued for 180 s with flow field information being output every 0.2 s for statistical analysis. In the following analysis of this test case, the mean value of a variable f is obtained by means of time averaging and is denoted by \bar{f} . The fluctuation of f is defined as $f' = f - \bar{f}$.

Figure 1 shows the vertical profiles of time-averaged streamwise velocity \bar{u} at the central cross-section of the turbine wake. LES results at $x/D = 2$ and 5 are shown and are compared with the inflow velocity profile at $x/D = -1$. The wind-tunnel measurement data from Ref. 9 is plotted for comparison. Using the actuator-disk model of wind turbine, the current LES captures the velocity deficit in the wake behind the turbine rotor ($0.33 < z/D < 1.33$, with the center of turbine rotor at $z/D = H_{\text{hub}}/D = 0.83$). The magnitude of velocity deficit obtained by the current LES agrees with the measurement data except in the near turbine region [Fig. 1(a)], where the LES result shows a relatively flat velocity profile. This flattening is caused by the use of the disk-averaged reference velocity in the actuator-disk model when calculating the turbine-induced force [see Eq. (4)]. Similar result has also been reported by Wu and Porté-Agel.⁸ A further consequence of the uniformly

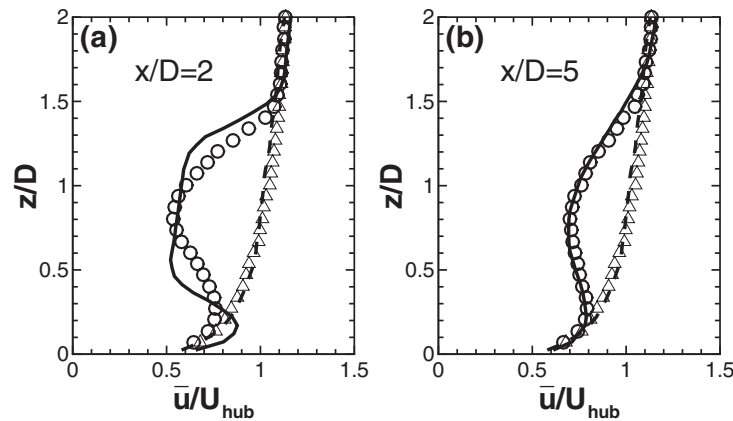


FIG. 1. Vertical profiles of time-averaged velocity \bar{u} at the central cross-section of the wake behind a single turbine at two downstream locations: (a) $x/D = 2$; and (b) $x/D = 5$. Here, D is the diameter of the turbine rotor, and U_{hub} is the mean inflow velocity (measured at $1D$ upstream of wind turbine hub). The wind tunnel measurement data of Chamorro and Porté-Agel⁹ is denoted by \circ , and the current LES result is denoted by —. In both (a) and (b), the inflow profile (at $x/D = -1$) is also plotted as a reference: Δ , data from Chamorro and Porté-Agel;⁹ ---, current LES result.

distributed blockage across the disk in the actuator disk model is an acceleration below the turbine rotor height seen in Fig. 1(a) between $z/D = 0.1$ and 0.25 . This is due to flow deflection towards the region underneath the turbine, which leads to a velocity that even slightly exceeds the incoming velocity at that height. However, these deviations from the measured mean flow are then mixed rather efficiently by the turbulence, and at the further downstream locations [Fig. 1(b)], the mean wind velocity profile obtained by the LES agrees very well with the wind-tunnel measurement data. Due to the turbulent mixing, the mean velocity at hub height recovers and increases to $0.70 U_{\text{hub}}$ at $x/D = 5$, compared with $0.56 U_{\text{hub}}$ at $x/D = 2$. Note that the inflow profile at $x/D = -1$ from the current LES agrees with the inflow profile in the measurement and shows no velocity deficit, which indicates that the streamwise domain size in the LES is sufficient for this test case.

Figure 2 shows the vertical profiles of u'^{rms} at $x/D = 2$ and 5 . Here, the superscript “rms” denotes the abbreviation of root mean square. At $x/D = 2$ [Fig. 2(a)], there exist two peaks in the u'^{rms} curve at $z/D = 0.33$ and 1.33 , respectively, corresponding to the lower and upper edges of the wind turbine wake region, respectively. The value and location of the upper peak from the LES agree with the measurement data. As expected, the resolved variance in LES is an underestimate of the

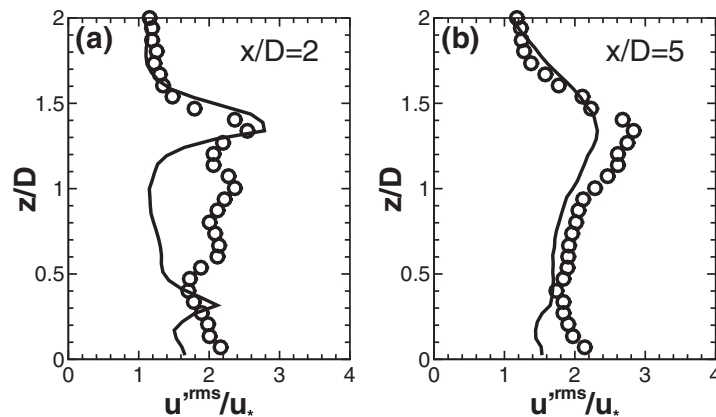


FIG. 2. Vertical profiles of u'^{rms} at the central cross-section of the wake behind a single turbine at two downstream locations: (a) $x/D = 2$; and (b) $x/D = 5$. Here, D is the diameter of the turbine rotor, and u_* is the wind friction velocity. The wind tunnel measurement data of Chamorro and Porté-Agel⁹ is denoted by \circ , and the current LES result is denoted by —.

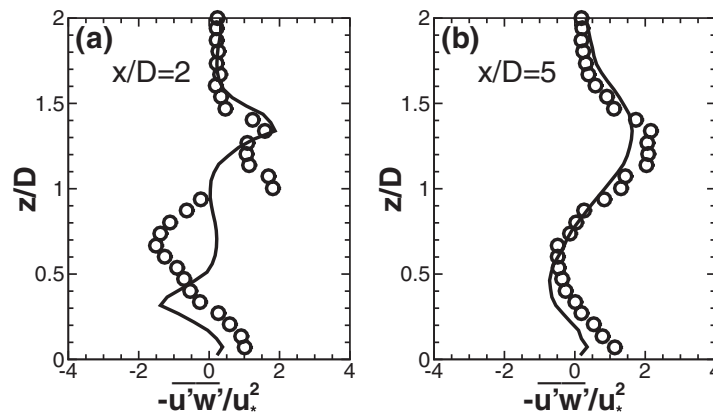


FIG. 3. The same as in Fig. 2 but for profiles of $-\overline{u'w'}$.

true rms since it does not include the subgrid-scale kinetic energy contribution. Near the center of the wake region, because of the flattening of the \bar{u} profile shown in Fig. 1(a), the current LES with the actuator-disk model obtains smaller value for u'^{rms} . At $x/D = 5$ [Fig. 2(b)], both the LES and the measurement obtain a single peak for u'^{rms} , for which the agreement is good.

Figure 3 shows the vertical profiles of $-\overline{u'w'}$ at $x/D = 2$ and 5. Because of the change of sign for the slope of \bar{u} , the value of Reynolds stress $-\overline{u'w'}$ in the turbine wake has opposite sign at higher and lower elevations, with positive value above and negative value below the hub height. At $x/D = 2$ [Fig. 3(a)], the current LES result shows strong positive and negative peaks of $-\overline{u'w'}$, with the magnitudes agreeing with the measurement data. Because of the flat \bar{u} profile shown in Fig. 1(a), the current LES shows smaller Reynolds stress near the hub height and a lower location of the negative peak compared with the measurement data. Similar results have also been reported by Wu and Porté-Agel⁸ in their simulation. At $x/D = 5$ [Fig. 3(b)], the profile of $-\overline{u'w'}$ obtained by the current LES agrees well with the measured profile in Ref. 9. Because of the recovery of wind velocity and the turbulent mixing, both the positive and negative peaks of $-\overline{u'w'}$ in the turbine wake become less pronounced as the distance from the wind turbine increases.

The results in the above test show that the actuator-disk model captures the essential flow physics in the wind turbine wake. We note that the details of the flow structure near the wind turbine rotor may not be fully resolved because of the modeling of the averaged effect of turbine rotor using an actuator disk. If the aerodynamics of the turbine blades and the associated tip vortices are the focus of the study, one should use other wind turbine models with more detailed turbine structure description, e.g., the actuator-line model⁴² and the curvilinear immersed boundary method.⁴³ However, those methods usually require much higher computational cost than the actuator-disk model. Moreover, the additional computational cost required to capture the wind-wave interaction using the present boundary-fitted and wave-following approach is appreciably higher than that for the simulation of flat land-based wind farm reported before. All of the above reasons make the actuator-disk model an appropriate choice for the LES of offshore wind farm in the present study.

The LES with actuator-disk model has been shown to be able to capture the essential physics in the interaction of large-scale wind farm with the atmospheric boundary layer.^{11,14,44} The performance of the current LES for large-scale wind farms is tested in Subsection III B.

B. Simulation of wind turbine array boundary layer

In this subsection, we test the current LES method by simulating a fully developed and land-based wind turbine array boundary layer. For validation, we match the simulation parameters with the cases A1 and A2 in Ref. 11. The simulation domain has a size of $(L_x, L_y, \bar{H}) = (\pi, \pi, 1.0)$ km. The domain contains a 4×6 aligned and evenly spaced turbine array, with the 4 turbine columns in the streamwise direction and the 6 turbine rows in the spanwise direction. The wind turbines have

a hub height of $H_{\text{hub}} = 100$ m and a rotor diameter of $D = 100$ m. The wind turbines thus have a streamwise spacing parameter of $s_x = (L_x/4)/D = 7.85$ and a spanwise spacing parameter of $s_y = (L_y/6)/D = 5.24$. The bottom boundary is flat and has a surface roughness of 0.1 m. The wind friction velocity is $u_* = 0.45$ m/s. In the LES, the grid resolution is $N_x \times N_y \times N_z = 128^3$, with evenly spaced grid in all of the three directions. The simulation is conducted using a timestep of 0.2 s. After a statistically steady state has been reached, the simulation is continued for 215 min with the three-dimensional flow field being output every 40 s for statistical analyses.

For validation, the result of the current LES is compared with the results of the cases A1 and A2 in Ref. 11, which have the same physical parameters but were simulated separately using two other codes (denoted as JHU-LES and KULEuven codes). In particular, the JHU-LES code uses pseudo-spectral discretization in the horizontal directions and second-order finite differencing in the vertical direction; a second-order Adams–Bashforth scheme is employed for time integration; the SGS stress is modeled by the LASD model;²⁸ the reference wind velocity $\langle \bar{u}^T \rangle_d$ is evaluated with a temporal-averaging window of $T = 0.27\bar{H}/u_*$. The KULEuven code uses pseudo-spectral discretization in the horizontal directions and fourth-order energy-conservative finite differencing in the vertical direction; a four-stage fourth-order Runge–Kutta scheme is used for time integration; the SGS stress is modeled by a standard Smagorinsky model⁴⁵ with a constant coefficient $C_s = 0.14$; the reference wind velocity $\langle \bar{u}^T \rangle_d$ is evaluated with a temporal-averaging window of $T = 0.6\bar{H}/u_*$. Note that the current LES code and the JHU-LES and KULEuven codes are developed independently. The JHU-LES and KULEuven codes were successfully used in several previous studies of flat land-based wind farms.^{11,33,46–48} Considering the significantly increased complexity in the current LES code associated with mobile sea surface and grid mapping (see Sec. II A), it is necessary to first compare the results of the current LES with those from JHU-LES and KULEuven codes for a flat-surface case.

For the statistical analysis of wind turbine array boundary layer, we define two different averaging operators for the velocity field: time averaging, denoted by the overbar \bar{u}_i ; and horizontal averaging, denoted by the brackets $\langle u_i \rangle$. The fluctuating velocity due to temporal variation is defined as $u'_i = u_i - \bar{u}_i$. The fluctuating velocity due to both temporal and spatial variations is defined as $u''_i = u_i - \langle \bar{u}_i \rangle$. Under statistically steady state, applying both the time and horizontal averaging operators to Eq. (1) gives¹¹

$$0 = -\frac{1}{\rho} \frac{\partial p_\infty}{\partial x} + \frac{\partial}{\partial z} \left(-\langle \bar{u}'w' \rangle - \langle \bar{u}''w'' \rangle \right) + \langle \bar{f}_T \rangle. \quad (19)$$

Here, $-\langle \bar{u}'w' \rangle$ is the averaged Reynolds shear stress; and $-\langle \bar{u}''w'' \rangle$ is the dispersive (or canopy) shear stress that indicates the correlation between the spatial inhomogeneities of \bar{u} and \bar{w} .⁴⁹ As illustrated in Fig. 4, the presence of wind turbine array induces appreciable spatial inhomogeneity, so that the dispersive stress is expected to have non-negligible contribution to the total shear stress.¹¹

Figure 5 shows the vertical profile of the time- and horizontal-averaged velocity. The mean velocity profile obeys the logarithmic law (indicated by the straight profile shape when plotted in the semi-logarithmic scale) below and above the turbine rotor region. The velocity deficit due to the presence of wind turbine array can be clearly seen in the turbine rotor region. The comparison

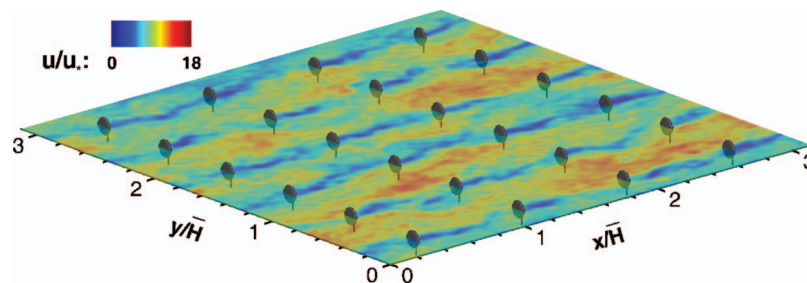


FIG. 4. Instantaneous streamwise velocity (normalized by u_*) on the horizontal plane at the wind turbine hub height, obtained from the current LES. The simulation parameters match those in cases A1 and A2 of Ref. 11.

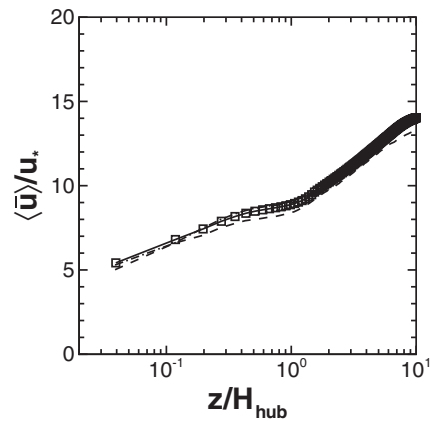


FIG. 5. Comparison of the profiles of time- and horizontal-averaged wind velocity $\langle \bar{u} \rangle$: ---, LES-JHU of Calaf *et al.*;¹¹ - · -, LES-KULEuven of Calaf *et al.*;¹¹ and \square -, current LES.

indicates only slight difference in the mean velocity profiles obtained by the three codes, which is caused by the difference in the numerical details of each code as discussed at the beginning of this subsection and in Sec. II A. Nevertheless, the mean velocity profile obtained from the current LES agrees well with those from the other two codes.

Figure 6 shows the vertical profiles of the Reynolds shear stress $-\langle \overline{u'w'} \rangle$, the dispersive shear stress $-\langle \overline{u''w''} \rangle$, and their sum. The results from all of the three LES codes show consistently that the Reynolds stress dominates at all the heights; the value of the dispersive stress is relatively small but not negligible. Moving away from the top boundary, the Reynolds stress obtained by the current LES first increases almost linearly, reaches its maximum at the upper edge of the turbine rotor region, decreases rapidly over the wind turbine region, and then decreases to zero at the bottom boundary. On the other hand, the dispersive stress obtained by the current LES increases nearly linearly from the top boundary, rapidly increases across the top edge of the rotor region and reaches its maximum around $z = 0.125\bar{H} = 1.25D$, and then gradually decreases to zero at the bottom boundary.

The Reynolds and dispersive stresses obtained by the current LES show profiles consistent with those by the JHU-LES and KULEuven codes, with the value and location of the profile peaks agreeing well. However, differences of Reynolds and dispersive stresses among the three codes at higher height are noticeable. Coceal *et al.*⁵⁰ reported similar difference and suggested that it is

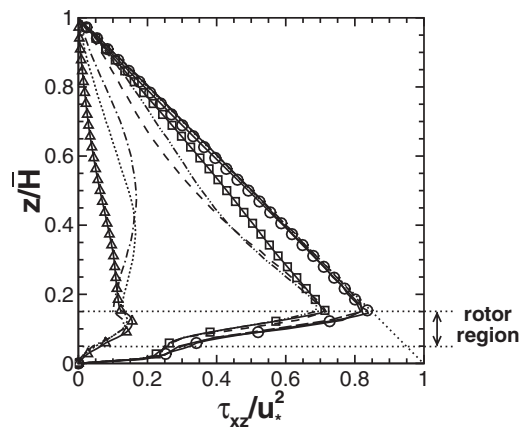


FIG. 6. Comparison of the profiles of shear stresses: · · ·, ---, and — denote, respectively, the dispersive, Reynolds, and total stresses of LES-JHU result of Calaf *et al.*;¹¹ · · ·, - · · -, and — denote, respectively, the dispersive, Reynolds, and total stresses of LES-KULEuven result of Calaf *et al.*;¹¹ and \triangle , \square , and \ominus denote the dispersive, Reynolds, and total stresses of the current LES, respectively. For the current LES, the symbols are shown for every four grid points.

caused by the different number of time frames used for the statistical analysis. Less time frames for averaging tends to give larger dispersive stress and smaller Reynolds stress in the outer layer. In the present study, we paid special attention to having sufficient samples in the statistics for the accuracy in the results. The total shear stress obtained by all of the three LES codes agrees well, showing a linear behavior towards 1 for its normalized value from the top boundary till the top edge of the wind turbine region. Within the turbine region, additional momentum loss is induced by the turbine forcing and causes the rapid decrease of the total stress. Figure 6 shows that all of the three LES codes accurately capture the stress balance indicated by Eq. (19), which is critically important for the study of wind turbine array boundary layers.

IV. LES OF OFFSHORE WIND FARM

A. Problem setup

For the simulation of offshore wind farm, we consider a turbulent wind turbine array boundary layer over an open sea area. For the sea-surface wave field, we consider both fetch-limited and fully developed sea conditions. For a wind-sea with limited fetch (defined as the distance of waves being blown by wind, and denoted by F), we use the wave spectrum obtained during the Joint North Sea Wave Observation Project (JONSWAP).³¹ Its one-dimensional spectral form in wavenumber space is described by

$$S_J(k) = \frac{\alpha_J}{2k^3} \exp \left[-\frac{5}{4} \left(\frac{k_p}{k} \right)^2 \right] \gamma^r. \quad (20)$$

Here, k_p is the wavenumber of the spectrum peak; and α_J , γ , and r are the spectrum parameters. For a fully developed sea, its surface wave field satisfies the Pierson–Moskowitz (P–M) spectrum:³²

$$S_{pm}(k) = \frac{\alpha_{pm}}{2k^3} \exp \left[-1.69\beta_{pm} \left(\frac{k_p}{k} \right)^2 \right], \quad (21)$$

where α_{pm} and β_{pm} are the spectrum parameters. Details of the JONSWAP and P–M spectra, including the values of the spectrum parameters, are given in Appendix B. The environmental wind field (before encountering the wind farm) has a mean wind velocity of $U_{10} = 12.5$ m/s at the height of 10 m above the mean water level. The key parameters of the corresponding wave fields for the given wind condition are listed in Table I. We remark that waves of different wavelengths propagate at different phase speeds, resulting in different form drags and rates of wind–wave momentum transfer and cannot be simply estimated based on the wave height information (e.g., the significant wave height h_s in Table I).^{18,51}

For a three-dimensional sea-surface wave field, the spreading of the waves satisfies a directional function⁵²

$$\chi(k, \theta) = \begin{cases} \mathcal{N}(s) \cos^{2s} \left(\frac{\pi}{\Theta} \theta \right), & |\theta| \leq \frac{\Theta}{2}, \\ 0, & |\theta| > \frac{\Theta}{2}. \end{cases} \quad (22)$$

TABLE I. Parameters of wave spectra for the HOSM simulations. Here, U_{10} is the mean wind velocity at the height of 10 m above the mean water level; and F is the distance over which the wind has been blowing the water surface. At the peak of the wave spectra (denoted by the subscript “p”), λ_p is the wavelength; ω_p is the wave angular frequency; c_p is the wave phase speed, and h_s is the significant wave height.

| Wave spectrum | U_{10} (m/s) | F (km) | λ_p (m) | k_p (m^{-1}) | ω_p (s^{-1}) | c_p (m/s) | h_s (m) |
|---------------|----------------|----------|-----------------|---------------------------|--------------------------------|-------------|-----------|
| JONSWAP | 12.5 | 80.0 | 60.0 | 0.1 | 1.0 | 9.7 | 1.8 |
| P–M | 12.5 | ∞ | 150.0 | 0.04 | 0.6 | 15.3 | 3.9 |

Here, Θ is the range of the spreading angle; s is the spreading parameter; and $\mathcal{N}(s)$ is the normalizing constant, with which $\chi(k, \theta)$ satisfies the constraint

$$\int_{-\pi}^{\pi} \chi(k, \theta) d\theta = 1. \quad (23)$$

In the present study, we use $\Theta = \pi$ and $s = 1.0$, which gives $\mathcal{N}(s) = 2/\pi$ based on Eq. (23). The corresponding directional wave spectra for the JONSWAP and P-M cases are obtained as

$$S^*(k, \theta) = S(k)\chi(k, \theta). \quad (24)$$

Based on Eqs. (20)–(24) and the parameters in Table I, the initial three-dimensional ocean broadband wave field for the HOSM simulation is generated using a random phase method.²⁵ Starting from linearly superposed wave modes (based on the wave spectra), after an initial adjustment period,⁵³ the HOSM is able to capture the nonlinear interaction among different wave modes and the nonlinearity in sea-surface geometry,^{24,38,54} and maintain the correct sea-surface wave spectra.^{55–57}

For the LES of offshore wind farm, we consider an $N_{\text{row}} \times 3$ wind turbine array within the simulation domain, which is a periodic representation of a large wind farm under fully developed condition. Here, N_{row} is the number of turbine rows (in the streamwise direction) in the simulation domain, and three values of $N_{\text{row}} = 2, 3$, and 4 are considered in this study. The wind turbines have a hub height of $H_{\text{hub}} = 100$ m and a rotor diameter of $D = 100$ m. The computational domain of the LES has a size of $(L_x, L_y, \bar{H}) = (2.1, 1.5, 1.0)$ km, so that the streamwise wind turbine spacing parameter is $s_x = (L_x/N_{\text{row}})/D = 10.5, 7.0$, and 5.25 for $N_{\text{row}} = 2, 3$, and 4, respectively; and the spanwise spacing parameter has a fixed value of $s_y = (L_y/3)/D = 5.0$. Note that Calaf *et al.*¹¹ have shown that a domain height of $\bar{H} = 1.0$ km is sufficient for capturing the essential flow physics in a wind farm with $H_{\text{hub}} = 100$ m, and doubling the domain height to 2.0 km results in negligible difference (see Fig. 2(b) in Ref. 11). Similarly, a ratio of $\bar{H}/H_{\text{hub}} = 8.75\text{--}10.0$ has been used in several studies and is found to provide satisfactory results.^{14,33,34,44}

The bottom of the wind field is bounded by sea-surface waves, and a proper value needs to be used for the subgrid-scale sea-surface roughness z_0 . For wind over pure wind-sea and assuming equilibrium between wind and short waves, the total sea-surface roughness may be parameterized by the classical Charnock relation $z_{0,\text{total}} = \alpha_{ch} u_*^2/g$.⁵⁸ However, the Charnock constant α_{ch} is an empirical coefficient, which has significant variations under various wind and wave conditions even without the presence of offshore wind turbine array.⁵⁹ Moreover, the difference between z_0 and $z_{0,\text{total}}$ corresponds to the overall effect of sea-surface waves that is resolved by LES, which is not known in advance. We note that a recently developed dynamic approach^{57,60} to determine z_0 can be used but is left for future tests. Instead, for clarity, in this study we use a non-dynamic prescribed value of 2.0×10^{-4} m for the subgrid-scale roughness z_0 , which is consistent with typical observed values and has been used in previous LES of wind over sea-surface waves.^{18,23} The key parameters of the offshore wind turbine array for the various cases are summarized in Table II. For each turbine array configuration, a flat-surface case is also considered.

For the LES, we use a grid resolution of $N_x \times N_y \times N_z = 192 \times 128 \times 192$, with evenly spaced grid in all of the three directions. For the HOSM, as explained in Sec. II B, a higher grid resolution of $N_x \times N_y = 512 \times 384$ is used to resolve the energy-containing wave modes in the spectra. (Note that HOSM does not require an explicit spatial discretization in the vertical direction.⁵⁴) The simulation is advanced in time using a timestep of 0.08 s. At the initial stage of the simulation, the wind turbine model is turned off and a pure wind–wave coupled flow is simulated based on the parameters in Table I. When the wind and wave fields reach a statistically steady state, the wind turbine model is turned on gradually over a relaxation period of 10 min. During this relaxation process and an additional 50 min of adjusting period, the imposed pressure gradient Π in Eq. (1) is fine-tuned to approach another constant value so that the mean velocity at the top boundary U_{top} remains constant. As a result, the wind turbine array boundary layer satisfies the desired geostrophic wind condition.¹¹ The simulation then continues till a statistically steady state is reached. After that, the simulation is continued for about 135 min with the three-dimensional flow field being output every 8 s for statistical analyses. An example of the results of cases J3 and PM3 is shown in Fig. 7.

TABLE II. Physical parameters of the various LES cases for land-based and offshore wind farms. The second column “BBC” denotes the type of bottom boundary condition for the wind farm.

| Case | BBC | N_f | s_x | s_y | H_{hub} (m) | D (m) | z_0 (m) | (L_x, L_y, \bar{H}) (m) |
|------|---------|--------------|-------|-------|----------------------|----------------------|-------------------------------|-------------------------------|
| FS | Flat | 1 | 28.8 | 4.8 | 0.125 | 0.15 | 3.0×10^{-5} | (4.32, 0.72, 0.46) |
| FA | Flat | 4×6 | 7.85 | 5.24 | 100.0 | 100.0 | 0.1 | $(\pi, \pi, 1.0) \times 10^3$ |
| J2 | JONSWAP | 2×3 | 10.5 | 5.0 | 100.0 | 100.0 | 2.0×10^{-4} | $(2.1, 1.5, 1.0) \times 10^3$ |
| J3 | JONSWAP | 3×3 | 7.0 | 5.0 | 100.0 | 100.0 | 2.0×10^{-4} | $(2.1, 1.5, 1.0) \times 10^3$ |
| J4 | JONSWAP | 4×3 | 5.25 | 5.0 | 100.0 | 100.0 | 2.0×10^{-4} | $(2.1, 1.5, 1.0) \times 10^3$ |
| PM2 | P-M | 2×3 | 10.5 | 5.0 | 100.0 | 100.0 | 2.0×10^{-4} | $(2.1, 1.5, 1.0) \times 10^3$ |
| PM3 | P-M | 3×3 | 7.0 | 5.0 | 100.0 <td 100.0 | 2.0×10^{-4} | $(2.1, 1.5, 1.0) \times 10^3$ | |
| PM4 | P-M | 4×3 | 5.25 | 5.0 | 100.0 | 100.0 | 2.0×10^{-4} | $(2.1, 1.5, 1.0) \times 10^3$ |
| FL2 | Flat | 2×3 | 10.5 | 5.0 | 100.0 | 100.0 | 2.0×10^{-4} | $(2.1, 1.5, 1.0) \times 10^3$ |
| FL3 | Flat | 3×3 | 7.0 | 5.0 | 100.0 | 100.0 | 2.0×10^{-4} | $(2.1, 1.5, 1.0) \times 10^3$ |
| FL4 | Flat | 4×3 | 5.25 | 5.0 | 100.0 | 100.0 | 2.0×10^{-4} | $(2.1, 1.5, 1.0) \times 10^3$ |

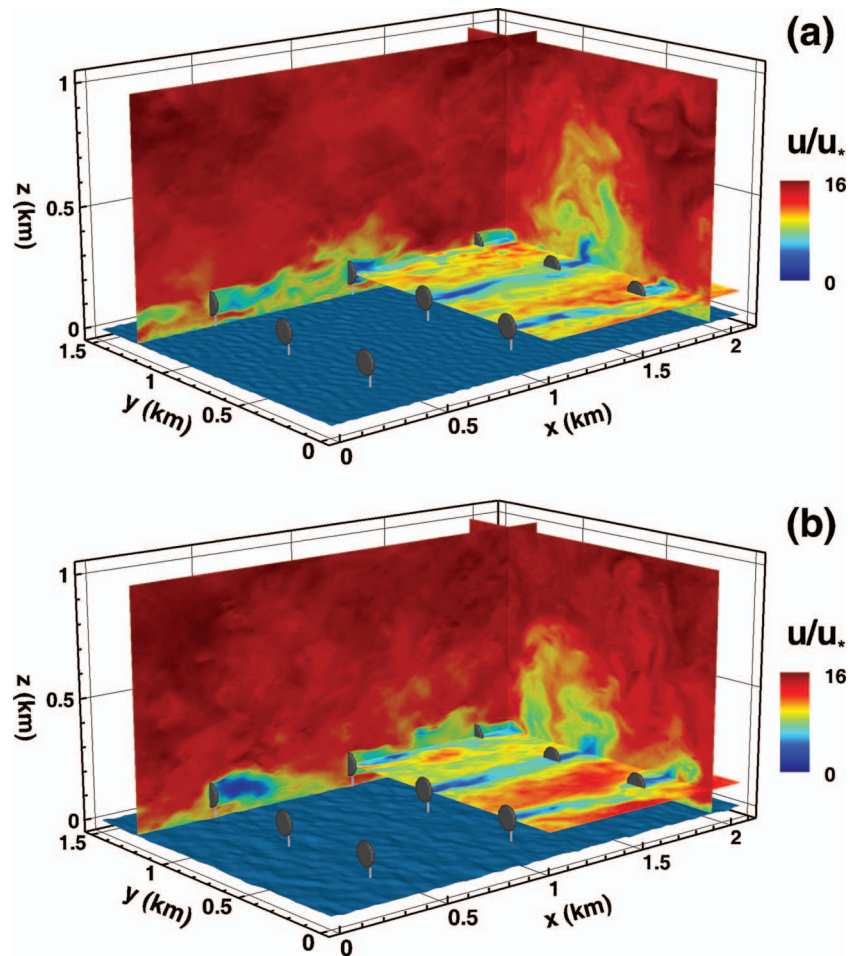


FIG. 7. Illustration of three-dimensional flow field in the fully developed wind turbine array boundary layer over water waves for cases (a) J3 and (b) PM3. Contours of instantaneous streamwise velocity u (normalized by u_*) are plotted on the three representative planes. In particular, the (x, z) -plane is chosen to cross the central line of the third wind turbine column; the (y, z) -plane is chosen to be at 1.86 turbine-diameter downstream of the third turbine row; and the (x, y) -plane is chosen to be at the hub height. For the visualization of sea-surface waves, only half of the (x, y) -plane is shown.

We note that after the wind and wave fields encounter the offshore wind farm, the wind speed near the sea surface is reduced. Thus the waves near the spectrum peak propagate a bit faster than the wind. Therefore, within the wind farm region, the sea-surface wave field is effectively in a “fully developed” condition for both the JONSWAP and P–M cases.³² Under such condition, the wave field is able to maintain its basic spectral form without significant growth or decay. Thus the horizontally periodic boundary condition for both the wind farm and the wave field is a reasonable treatment in the current LES.

B. General statistics of offshore wind turbine array boundary layer

Figure 8 shows the averaged streamwise velocity spectra at different heights obtained by the simulations for cases J3 and PM3. The spectra are calculated through one-dimensional Fourier transform of u in the streamwise direction, and then averaged both in the spanwise direction and in time. The spectra are normalized with u_* and z and plotted as a function of $k_x z$. As shown in Fig. 8, near the wave surface ($z/H_{\text{hub}} = 0.03$ and 0.50), the spectra of streamwise velocity scale approximately as k_x^{-1} in the production range ($k_x z < 1.0$); above the top of the turbine region ($z/H_{\text{hub}} > 1.5$), the wind turbulence is nearly isotropic, and the spectra of the streamwise velocity scale as $k_x^{-5/3}$ in the initial subrange ($k_x z > 1.0$). The above results agree well with the LES result of Bou-Zeid *et al.*²⁸ (for a neutral atmospheric boundary layer over land) and the experimental result Cal *et al.*¹³ (for a land-based wind turbine array boundary layer), indicating that the current LES with the LASD model of SGS stress captures the characteristics of turbulence energy cascade well. Moreover, Fig. 8 shows a shift of streamwise velocity spectra to higher values over the turbine region (from $z/H_{\text{hub}} = 0.5$ to 1.5), indicating the enhancement of turbulence level induced by the wind–turbine interaction.

Figure 9 shows the time-averaged three-dimensional flow field for case PM3. Note that the time averaging of the wave surface elevation results in an almost flat bottom boundary in Fig. 9. As shown in Fig. 9(a), the actuator-disk model clearly induces a wake region behind the turbine rotor. This turbine wake region extends over $5D$ in the downstream direction, where the velocity deficit recovers gradually due to turbulence mixing. At the edge of the wake region, there exists a shear layer, where the wind velocity becomes smaller towards the center line of the turbine wake and larger towards the outer side of the wake region. The slopes of the mean velocity profile have opposite signs at the upper and lower edges of the turbine rotor region, resulting in two high Reynolds stress regions with opposite signs starting from the rotor tip in the downstream direction [Fig. 9(b)]. Within the

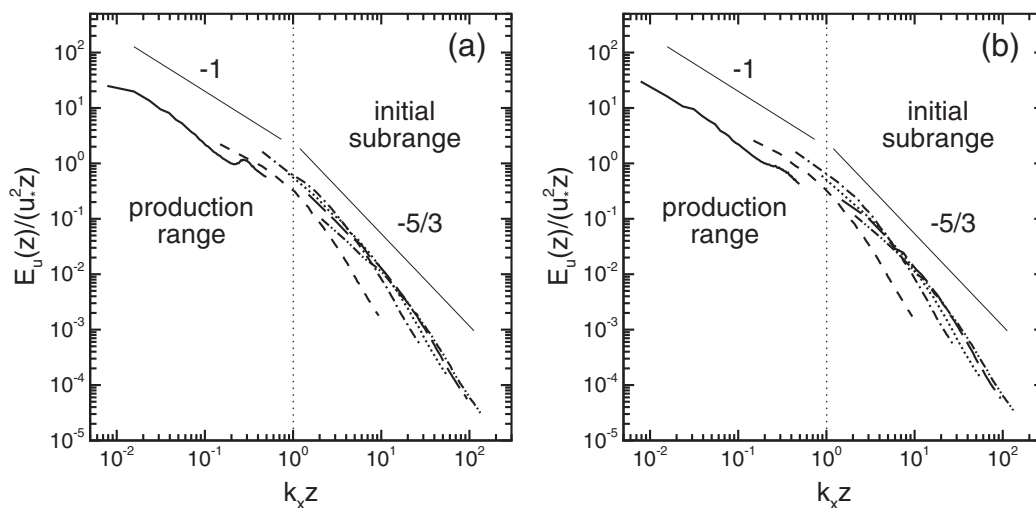


FIG. 8. Normalized streamwise wind velocity spectra as a function of $k_x z$ for cases (a) J3 and (b) PM3. The colored lines with different patterns represent the spectra obtained at various heights of $z/H_{\text{hub}} = : 0.03$ (—); 0.50 (---); 1.49 (- · - ·); 3.01 (· · · ·); 5.00 (- - -); and 7.04 (- · · ·). The -1 slope for the production range ($k_x z < 1.0$) and the $-5/3$ slope for the initial subrange ($k_x z > 1.0$) are also shown.

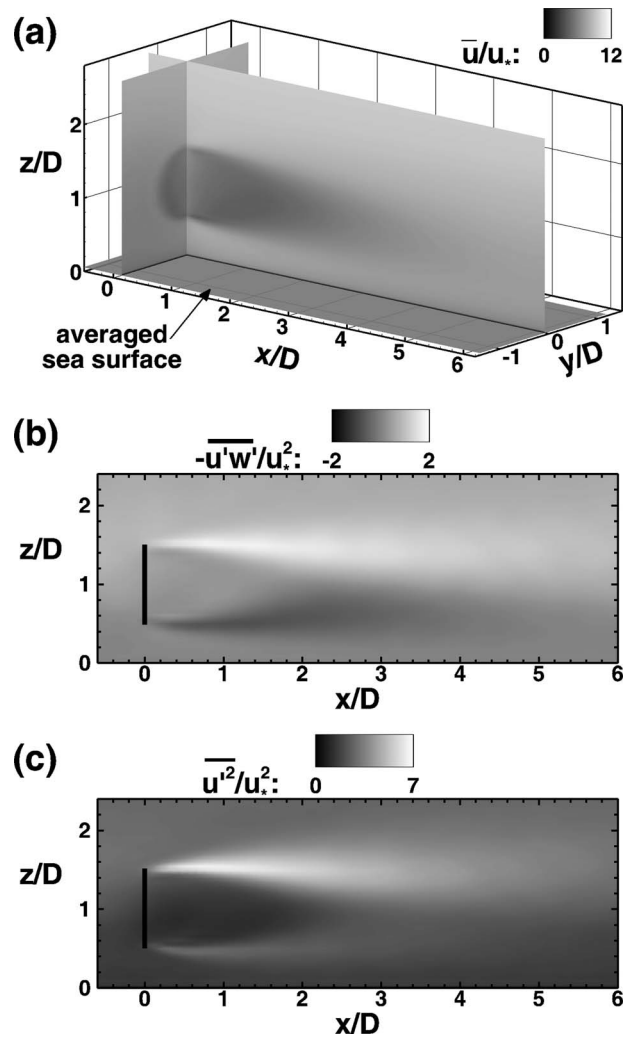


FIG. 9. Time-averaged wind field in the turbine wake for the P-M wave case: (a) streamwise velocity \bar{u} ; (b) Reynolds stress $-\overline{u'w'}$; and (c) variance of streamwise velocity $\overline{u'^2}$. In (a), both the (y, z) -plane at the turbine disk and the (x, z) -plane across the center of the turbine disk are shown; in (b) and (c), the (x, z) -plane across the center of the turbine disk are shown.

shear layer, the turbulence intensity is also high [Fig. 9(c)] due to the high turbulence production associated with the large Reynolds stress and strong shear rate. Moreover, unlike the turbulence wake in a uniform incident flow, the boundary layer flow in the current LES has higher velocity at higher elevation. Thus the magnitudes of Reynolds stress and turbulence intensity are higher along the upper tip of the turbine rotor than those along the lower tip, as shown in Figs. 9(b) and 9(c). This result agrees with the measurements in Vermeer *et al.*⁴ (see their Fig. 35) and Cal *et al.*¹³ (see their Fig. 10).

The Lagrangian feature of the LASD SGS model used in the current study enables the three dimensional variation of the Smagorinsky coefficient, and is expected to represent the turbulence statistics better than models using planar averaging, particularly for complex flows such as the current wind-turbine interaction problem. Figure 10 shows the time-averaged Smagorinsky coefficient C_s for the case PM3. The value of C_s is high within the turbine wake around the hub height, a trend for which we do not have a ready physical explanation. Towards the edges of the turbine rotor region as well as towards the sea surface, the value of C_s decreases due to the large shear rate and the strong anisotropy of the wind turbulence associated with coherent turbulence structures⁶¹ as well

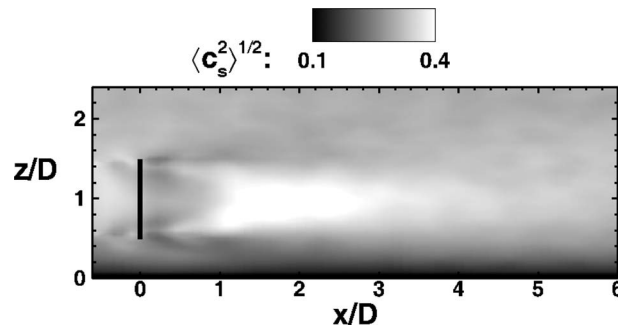


FIG. 10. Time-averaged dynamic Smagorinsky coefficient $\langle C_s^2 \rangle^{1/2}$ for the case PM3 in the (x, z) -plane across the center of the turbine disk.

as wall-blocking effects near the surface. Similarly, the value of C_s is small in the near wake of the wind turbine due to the flow anisotropy caused by the presence of turbine rotor.

We remark that the time-averaged flow fields for various wave conditions and turbine spacings show qualitatively similar characteristics as the results in Figs. 9 and 10. Meanwhile, the sea-surface waves and turbine spacing have appreciable effects on the statistical values of the wind turbine array boundary layer, which are discussed in Subsections IV C–IV E.

C. Effects of wave condition and turbine spacing on mean velocity profile

Figure 11 shows the mean velocity profiles of the various offshore wind farm cases listed in Table II. To calculate the mean velocity profile, the instantaneous velocity obtained on the boundary-fitted computational grid is first interpolated to a Cartesian grid in physical space, and then averaged over each horizontal plane as well as over time. Note that the evaluation of velocity on the Cartesian grid only involves interpolation in the vertical direction, as indicated by the grid mapping in Eq. (12). In the vertical direction, the Cartesian grid has 193 points, which are evenly spaced between $z = 0$ and $z = \bar{H}$. For the Cartesian grid points that are located between the instantaneous sea surface and the first boundary-fitted grid above it, one-side logarithmic extrapolation is used because of the

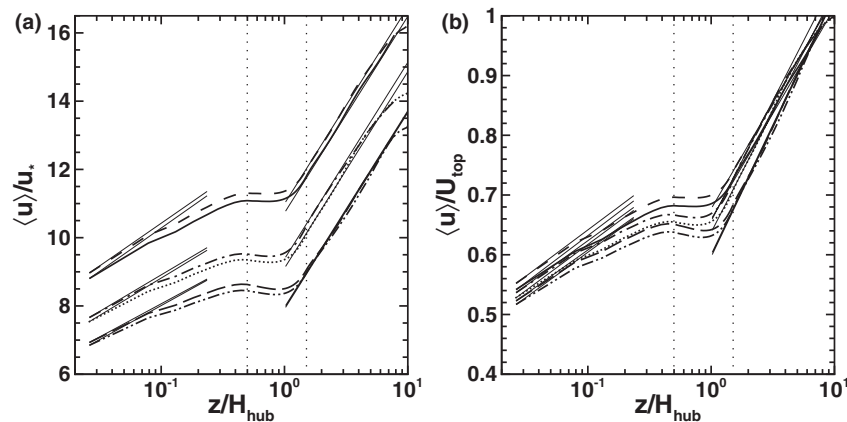


FIG. 11. Mean velocity profiles for offshore wind farms normalized by (a) u_* and (b) U_{top} for different wave conditions and turbine spacing: —, case J2; ···, case J3; - · - ·, case J4; - - -, case PM2; - · - ·, case PM3; and - - -, case PM4. The lower and upper bounds ($z/H_{\text{hub}} = 0.5$ and 1.5 , respectively) of the turbine region are indicated by vertical dotted lines. For each case, the corresponding logarithmic profiles are indicated by thin solid lines: below the turbines ($z/H_{\text{hub}} < 0.5$), $\langle \bar{u} \rangle = u_{*lo} \ln(z/z_{0,lo})/\kappa$; above the turbines ($z/H_{\text{hub}} > 1.5$), $\langle \bar{u} \rangle = u_{*hi} \ln(z/z_{0,hi})/\kappa$. Values for u_{*lo} and $z_{0,hi}$ are listed in Table IV.

TABLE III. Evaluation of sea-surface stress for different cases based on the LES data.

| Case | $\tau_s/\rho U_{\text{top}}^2$ | $\tau_p/\rho U_{\text{top}}^2$ | $\tau_{\text{total}}/\rho U_{\text{top}}^2$ |
|------|--------------------------------|--------------------------------|---|
| J2 | 5.18×10^{-4} | 2.02×10^{-4} | 7.20×10^{-4} |
| J3 | 5.06×10^{-4} | 2.06×10^{-4} | 7.12×10^{-4} |
| J4 | 4.85×10^{-4} | 2.00×10^{-4} | 6.85×10^{-4} |
| PM2 | 5.49×10^{-4} | 1.51×10^{-4} | 7.00×10^{-4} |
| PM3 | 5.33×10^{-4} | 1.49×10^{-4} | 6.82×10^{-4} |
| PM4 | 5.06×10^{-4} | 1.45×10^{-4} | 6.51×10^{-4} |
| FL2 | 5.81×10^{-4} | 0.0 | 5.81×10^{-4} |
| FL3 | 5.33×10^{-4} | 0.0 | 5.33×10^{-4} |
| FL4 | 5.16×10^{-4} | 0.0 | 5.16×10^{-4} |

large velocity gradient near the boundary [cf. Eq. (7)]; for the Cartesian grid points that are below the instantaneous sea surface, the instantaneous velocity value from the wave simulation is used; for elsewhere inside the air domain, a linear interpolation is used. Note that periodic boundary conditions are used in conjunction with a mean streamwise pressure gradient to drive the flow (see Sec. II A), and there is no inflow profile that enforces the flow rate in the simulation domain. The mean profile obtained from the LES is the result of the dynamic balance among imposed pressure gradient, sea-surface drag, and turbine-induced drag. Figure 11 shows that, as the streamwise turbine spacing s_x decreases, the normalized mean velocity profile shifts towards lower values due to the larger resistance caused by more turbines. Moreover, a comparison between the JONSWAP and P–M wave cases indicates that the sea-surface waves have noticeable effect on the wind turbine array boundary layer.

For wind blowing over waves, the total streamwise stress acting on the wind at the sea surface consists of two components, i.e.,

$$\tau_{\text{total}} = \underbrace{-\frac{\rho}{A} \iint_A \tau_{xz}^{SGS} dx dy}_{\tau_s} + \underbrace{\frac{1}{A} \iint_A \tilde{p}_s \frac{\partial \tilde{\eta}}{\partial x} dx dy}_{\tau_p}. \quad (25)$$

Here, τ_s is the surface shear stress, with τ_{xz}^{SGS} given by Eq. (5); τ_p is the wave form drag, with \tilde{p}_s being the air pressure acting on the wave surface; and A is the total horizontal sea-surface area in the simulation domain. Table III shows the sea-surface stress budget for the various LES cases. Compared with the corresponding P–M wave cases, the JONSWAP wave cases have slightly smaller shear stress but larger wave form drag and total surface stress. Note that the dominant waves in the P–M cases are longer than those in the JONSWAP cases. Based on the dispersion relation of water waves, the dominant waves in the P–M cases are faster. Faster waves have smaller relative velocity with respect to the wind above. As a result, P–M cases have less wave form drag than JONSWAP cases. The current LES result is consistent with the results of previous studies on wind–wave interaction, which showed that faster waves induce smaller resistance to the wind.⁵¹ Moreover, for a given wave condition, the turbine number per unit surface area increases as the streamwise turbine spacing s_x decreases (see Table II). This results in an increase of turbine-induced stress and consequently a decrease of total surface stress τ_{total} . On the other hand, if the sea-surface wave effect is neglected (i.e., cases FL2–FL4), the simulated surface shear stress is slightly larger than the values obtained from the corresponding wave-present cases. However, the contribution from the wave form drag is missed, resulting in significantly lower total (normalized) surface stress for the flat surface cases.

We can further deduce that the effective friction velocity of the wind near the sea surface, $u_{*10} = \sqrt{\tau_{\text{total}}/\rho}$, varies with the total surface stress when the turbine spacing and the wave condition change. Let $z_{0,10}$ be the effective total sea-surface roughness, its relation with the total surface

TABLE IV. Evaluation of friction velocities and effective roughness heights based on the LES data, and comparison with the models of Frandsen⁶² and Calaf *et al.*¹¹ For u_{*lo} and $z_{0,hi}$, the current simulation result is denoted by the superscript “LES;” the predictions by the Frandsen model [Eqs. (30) and (31)] are denoted by the superscript “Fran;” and the prediction by the Calaf–Meneveau–Meyers model [Eqs. (33) and (34)] are denoted by the superscript “CMM.”

| Case | u_{*lo}^{LES}/u_* | u_{*lo}^{Fran}/u_* | u_{*lo}^{CMM}/u_* | $z_{0,lo}/H_{hub}$ | $z_{0,hi}^{LES}/H_{hub}$ | $z_{0,hi}^{Fran}/H_{hub}$ | $z_{0,hi}^{CMM}/H_{hub}$ |
|------|---------------------|----------------------|---------------------|-----------------------|--------------------------|---------------------------|--------------------------|
| J2 | 0.441 | 0.316 | 0.432 | 8.96×10^{-6} | 1.37×10^{-2} | 2.55×10^{-2} | 1.06×10^{-2} |
| J3 | 0.381 | 0.285 | 0.367 | 9.48×10^{-6} | 2.62×10^{-2} | 3.71×10^{-2} | 2.32×10^{-2} |
| J4 | 0.347 | 0.261 | 0.324 | 9.82×10^{-6} | 4.23×10^{-2} | 4.90×10^{-2} | 3.80×10^{-2} |
| PM2 | 0.435 | 0.312 | 0.424 | 6.88×10^{-6} | 1.23×10^{-2} | 2.44×10^{-2} | 1.04×10^{-2} |
| PM3 | 0.373 | 0.280 | 0.358 | 7.00×10^{-6} | 2.35×10^{-2} | 3.58×10^{-2} | 2.28×10^{-2} |
| PM4 | 0.339 | 0.257 | 0.317 | 7.28×10^{-6} | 4.14×10^{-2} | 4.77×10^{-2} | 3.77×10^{-2} |
| FL2 | 0.393 | 0.298 | 0.391 | 2.17×10^{-6} | 1.15×10^{-2} | 2.05×10^{-2} | 0.97×10^{-2} |
| FL3 | 0.334 | 0.265 | 0.329 | 2.19×10^{-6} | 2.49×10^{-2} | 3.16×10^{-2} | 2.18×10^{-2} |
| FL4 | 0.300 | 0.241 | 0.289 | 2.24×10^{-6} | 3.97×10^{-2} | 4.33×10^{-2} | 3.65×10^{-2} |

stress is

$$\tau_{total} = \left[\frac{\kappa U_{z2}}{\ln(z_2/z_{0,lo})} \right]^2, \quad (26)$$

where U_{z2} and z_2 are, respectively, the averaged wind velocity and elevation at the first Cartesian grid above the sea surface. The value of $z_{0,lo}$ can thus be evaluated by rewriting Eq. (26) as

$$z_{0,lo} = z_2 \exp\left(-\frac{\kappa U_{z2}}{\sqrt{\tau_{total}}}\right). \quad (27)$$

The values of u_{*lo} and $z_{0,lo}$ for the various LES cases are listed in Table IV. The logarithmic profiles based on $\langle \bar{u} \rangle(z) = u_{*lo} \ln(z/z_{0,lo})/\kappa$ are also plotted in Fig. 11 for the region below the turbine layer.

The result shows that the P–M wave cases have smaller total sea-surface roughness than the corresponding JONSWAP cases, consistent with previous studies on sea-surface roughness (see the review by Toba *et al.*⁵⁹). The change of streamwise turbine spacing s_x results in only small change in $z_{0,lo}$. This is because the turbines affect the waves indirectly through the slight change of near surface wind velocity; and the response time of the waves to the wind forcing is much larger than that of the wind to the turbine forcing. For the flat-surface cases, there is no wave-induced contribution to the surface roughness, so that the estimated values of $z_{0,lo}$ from the LES results are consistent with the imposed z_0 .

Above the turbine layer, the mean velocity profiles obey another logarithmic law, which can be expressed as

$$\langle \bar{u} \rangle(z) = \frac{u_*}{\kappa} \ln\left(\frac{z}{z_{0,hi}}\right). \quad (28)$$

Here, $z_{0,hi}$ is the effective roughness for the wind above the turbine layer. Following Ref. 11, we evaluate its value by

$$z_{0,hi} = 2H_{hub} \exp\left(-\frac{\kappa \langle \bar{u} \rangle_{z=2H_{hub}}}{u_*}\right), \quad (29)$$

where $\langle \bar{u} \rangle_{z=2H_{hub}}$ is the mean velocity at $z = 2H_{hub}$ obtained from our LES data. The evaluated values of $z_{0,hi}$ are listed in Table IV. For a given wave condition, the value of $z_{0,hi}$ increases as the turbine spacing s_x decreases, because of the decrease in the value of $\langle \bar{u} \rangle_{z=2H_{hub}}/u_*$. When s_x is fixed, the value of $z_{0,hi}$ is larger for the JONSWAP case than that of the P–M case. For the various LES cases, the logarithmic profiles based on Eq. (28) are also plotted in Fig. 11 and show good agreement with the LES results.

Theoretically, Frandsen⁶² proposed a model for $(u_{*lo}, z_{0,hi})$ by assuming two logarithmic profiles, respectively, below and above the turbine layer, with matching condition at the hub height. His model

can be written as⁶²

$$u_{*lo} = u_* \frac{\ln(H_{hub}/z_{0,hi})}{\ln(H_{hub}/z_{0,lo})}, \quad (30)$$

$$z_{0,hi} = H_{hub} \exp \left(-\kappa \left[\frac{c_{ft}}{2} + \left(\frac{\kappa}{\ln(H_{hub}/z_{0,lo})} \right)^2 \right]^{-1/2} \right), \quad (31)$$

where

$$c_{ft} = \frac{\pi C_T}{4s_x s_y} \quad (32)$$

is the friction coefficient of the wind turbines.

Recently, Calaf *et al.*¹¹ improved Frandsen's model by assuming a third layer within the turbine region with the wake mixing effect included. They proposed a new model (hereinafter referred to as the Calaf–Meneveau–Meyers (CMM) model) as follows:

$$u_{*lo} = u_* \frac{\ln \left[\frac{H_{hub}}{z_{0,hi}} \left(1 + \frac{D}{2H_{hub}} \right)^{v_w^*/(1+v_w^*)} \right]}{\ln \left[\frac{H_{hub}}{z_{0,lo}} \left(1 - \frac{D}{2H_{hub}} \right)^{v_w^*/(1+v_w^*)} \right]}, \quad (33)$$

$$z_{0,hi} = H_{hub} \left(1 + \frac{D}{2H_{hub}} \right)^{v_w^*/(1+v_w^*)} \times \exp \left(- \left[\frac{c_{ft}}{2\kappa^2} + \left(\ln \left[\frac{H_{hub}}{z_{0,lo}} \left(1 - \frac{D}{2H_{hub}} \right)^{v_w^*/(1+v_w^*)} \right] \right)^{-2} \right]^{-1/2} \right), \quad (34)$$

where

$$v_w^* = \frac{\sqrt{\frac{1}{2} c_{ft} \langle \bar{u} \rangle} D}{\kappa u_* z} \quad (35)$$

is a nondimensional wake eddy viscosity in the turbine region. Following Ref. 11, we use an approximated form of $v_w^* \approx 28 \sqrt{\frac{1}{2} c_{ft}}$ over the turbine region.

The model values of u_{*lo} and $z_{0,hi}$ based on Eqs. (30)–(35) are listed in Table IV. Both models show trends consistent with the current LES results. When the turbine spacing s_x decreases, the friction coefficient c_{ft} increases [Eq. (32)]. This variation results in an increase of $z_{0,hi}$ [Eqs. (31) and (34)] and thus a decrease of u_{*lo} [Eqs. (30) and (33)]. On the other hand, for a fixed turbine spacing s_x , the larger value of $z_{0,lo}$ for the JONSWAP case results in a larger value of $z_{0,hi}$ [Eqs. (31) and (34)] than that in the P–M case. Meanwhile, the increment of $z_{0,hi}$ is not as much as that of $z_{0,lo}$, and thus results in a larger value of u_{*lo} for the JONSWAP case than the P–M case [Eqs. (30) and (33)]. The comparison indicates that the CMM model has better agreement with the LES results than Frandsen's model does. Considering the increasing complexity of the current problem that involves wind–wave interaction, the agreement between the current LES result and the CMM model is encouraging. For the flat-surface cases, the CMM model and the LES results show excellent agreement, with $u_{*lo}^{LES}/u_{*lo}^{CMM} = 1.01$ – 1.04 . Note that a further refined model has been proposed that can account for different effects of spanwise and streamwise spacing.¹⁴

D. Budget of mean kinetic energy

For large-scale wind farms, the wind power extraction by the turbines is supplemented by the vertical flux of kinetic energy from the atmospheric flow above.¹¹ Under fully developed condition,

the transport equation of the kinetic energy for the time- and horizontal-averaged flow can be obtained by multiplying the mean streamwise momentum equation (19) with $\langle \bar{u} \rangle$:

$$\underbrace{-\frac{1}{\rho} \frac{\partial p_\infty}{\partial x} \langle \bar{u} \rangle}_{W_p} + \frac{\partial}{\partial z} \underbrace{\left[(-\langle u'w' \rangle) - \langle \bar{u}''\bar{w}'' \rangle \langle \bar{u} \rangle \right]}_{\Phi_e} = \underbrace{\left(-\langle u'w' \rangle - \langle \bar{u}''\bar{w}'' \rangle \right)}_{\varepsilon_e} \frac{\partial \langle \bar{u} \rangle}{\partial z} - \underbrace{\langle f_T \rangle \langle \bar{u} \rangle}_{W_T}. \quad (36)$$

Here, W_p is the work (per unit time) done by the imposed pressure forcing; Φ_e is the vertical flux of the kinetic energy; ε_e is the dissipation of kinetic energy; and W_T is the work (per unit time) done by the wind turbine layer (which differs from the actual power extracted at the axis of the wind turbines, but provides a global estimate of available power that can be extracted in the wind-turbine layer).

The effect of turbine spacing on the terms in Eq. (36) has been studied by Calaf *et al.*¹¹ based on LES of land-based wind farms. Here, we focus on the study of sea-surface wave effect. The results of cases J3 and PM3 are plotted in Figs. 12–14. Figure 12 shows the vertical profile of the mean kinetic energy flux Φ_e . Away from the top boundary, the magnitude of Φ_e increases gradually and reaches its maximum at the upper edge of the turbine region. Across the turbine region, Φ_e decreases rapidly to a much lower value towards the lower edge. Thus, there is a net flux of mean kinetic energy to support the turbine-layer mean power W_T .^{11,13} Figure 12 shows that case PM3 has a larger value of Φ_e than case J3 as a result of the relatively larger wind velocity in case PM3.

Figure 13 shows the vertical profile of the turbine-layer mean power W_T . Because the turbine force f_T is none-zero only within the turbine layer [see Eq. (4)], the value of W_T is zero everywhere else except within the turbine layer. Meanwhile, due to the circular geometry of the turbine disk, the time- and horizontal-averaged turbine force $\langle f_T \rangle$ increases gradually from zero at the edges of the turbine layer to its peak value at the wake center, so does W_T . Similar to Φ_e , W_T is larger for case PM3 than case J3, because the wind velocity in case PM3 is larger.

Figure 14 shows the vertical profile of the dissipation term ε_e . The dissipation is significant near the sea surface, similar to other turbulent boundary layer flows. The presence of wind farm induces a second peak at the upper edge of the turbine region, where the Reynolds stress is large and the mean flow loses kinetic energy to produce turbulence [Figs. 9(b) and 9(c)]. The wave effect on the dissipation is found to be small.

The budget for the total mean kinetic energy within the turbine region can be obtained by integrating Eq. (36) over $z \in [H_{\text{hub}} - D/2, H_{\text{hub}} + D/2]$. This gives

$$W_p + \Delta \Phi_e = \mathcal{D} + W_T, \quad (37)$$

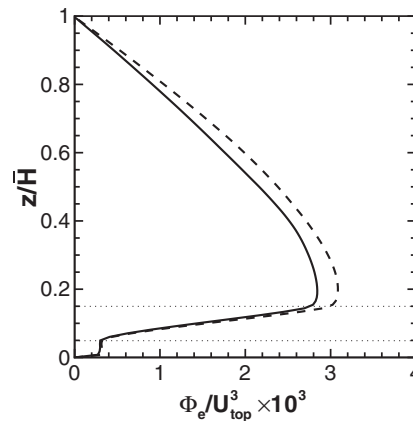


FIG. 12. Vertical profiles of fluxes of mean kinetic energy for: —, case J3; and — —, case PM3. The lower and upper bounds ($z/\bar{H} = 0.05$ and 0.15 , respectively) of the turbine region are indicated by dotted lines.

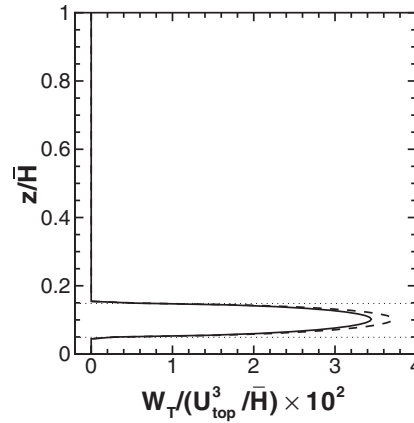


FIG. 13. Vertical profiles of turbine work for: —, case J3; and - - -, case PM3. The lower and upper bounds ($z/\bar{H} = 0.05$ and 0.15 , respectively) of the turbine region are indicated by dotted lines.

where

$$\mathcal{W}_p = -\frac{D}{\rho} \frac{\partial p_\infty}{\partial x} \langle \bar{u} \rangle_D, \quad (38)$$

$$\Delta \Phi_e = \Phi_e(H_{\text{hub}} + D/2) - \Phi_e(H_{\text{hub}} - D/2), \quad (39)$$

$$\mathcal{D} = \int_{H_{\text{hub}} - D/2}^{H_{\text{hub}} + D/2} (-\langle \bar{u}'w' \rangle - \langle \bar{u}''\bar{w}'' \rangle) \frac{\partial \langle \bar{u} \rangle}{\partial z} dz, \quad (40)$$

$$\mathcal{W}_T = -\frac{\pi C_T}{8s_x s_y (1-a)^2} \overline{\langle u^T \rangle_d^2} \langle \bar{u} \rangle_D. \quad (41)$$

Here,

$$\langle \bar{u} \rangle_D = \frac{1}{D} \int_{H_{\text{hub}} - D/2}^{H_{\text{hub}} + D/2} \langle \bar{u} \rangle dz \quad (42)$$

is the mean velocity of the turbine region; \mathcal{W}_p is the forcing power in the turbine region due to imposed pressure gradient; $\Delta \Phi_e$ is the net flux of kinetic energy into the turbine region; \mathcal{D} is the dissipation of mean kinetic energy in the turbine region; and \mathcal{W}_T is the loss of mean kinetic energy due to turbine work.

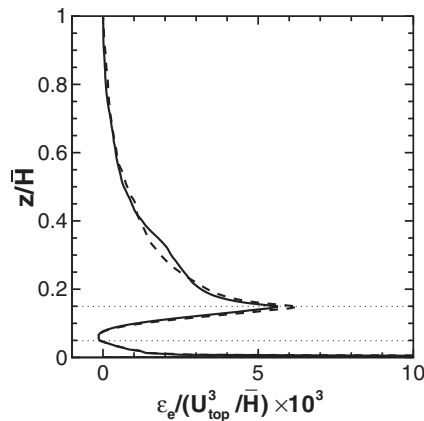


FIG. 14. Vertical profiles of dissipation of mean kinetic energy for: —, case J3; and - - -, case PM3. The lower and upper bounds ($z/\bar{H} = 0.05$ and 0.15 , respectively) of the turbine region are indicated by dotted lines.

TABLE V. Evaluation of total mean kinetic energy budget in the turbine region. All the values are normalized by U_{top}^3 . The relative residual error ϵ is calculated as $\epsilon = (\mathcal{W}_p + \Delta\Phi_e - \mathcal{D} - \mathcal{W}_T)/(\mathcal{D} + \mathcal{W}_T)$.

| Case | \mathcal{W}_p | $\Delta\Phi_e$ | \mathcal{D} | \mathcal{W}_T | ϵ |
|------|-----------------------|-----------------------|-----------------------|-----------------------|------------|
| J2 | 2.53×10^{-4} | 1.76×10^{-3} | 1.09×10^{-4} | 1.88×10^{-3} | 1.32 % |
| J3 | 3.27×10^{-4} | 2.47×10^{-3} | 1.80×10^{-4} | 2.60×10^{-3} | 0.40 % |
| J4 | 3.64×10^{-4} | 2.78×10^{-3} | 1.77×10^{-4} | 2.92×10^{-3} | 1.41 % |
| PM2 | 2.58×10^{-4} | 1.84×10^{-3} | 1.09×10^{-4} | 1.96×10^{-3} | 1.15 % |
| PM3 | 3.34×10^{-4} | 2.67×10^{-3} | 2.06×10^{-4} | 2.81×10^{-3} | 0.21 % |
| PM4 | 3.70×10^{-4} | 2.79×10^{-3} | 1.57×10^{-4} | 2.99×10^{-3} | 0.28 % |

The terms of total mean kinetic energy budget for the various cases are listed in Table V. In order to perform direct comparison, all of the values are normalized using U_{top} , representing consistent geostrophic wind condition.²⁷ For all of the cases, $\Delta\Phi_e$ and \mathcal{W}_T dominate and nearly balance with each other, while \mathcal{W}_p and \mathcal{D} are one order of magnitude smaller. This result is consistent with the LES result of the land-based wind farm in Ref. 11, which showed that the works done by the turbines inside a large wind farm are mainly supported by the vertical energy flux from the atmosphere above. For a given wave condition, the value of \mathcal{W}_T increases as the turbine spacing s_x decreases, because there are more working turbines per unit surface area. The increase of \mathcal{W}_T thus requires more energy supplement from the wind above the turbine layer, as shown by the larger value of $\Delta\Phi_e$ in Table V. On the other hand, for a fixed turbine spacing, the P–M wave cases show larger magnitude for both $\Delta\Phi_e$ and \mathcal{W}_T compared with the corresponding JONSWAP wave cases, due to the wave effect on the vertical profiles of Φ_e and W_T [Figs. 12 and 13]. For all of the LES cases in the current study, the relative residual error for the budget is within 1.5%, indicating that the flow field has reached a fully developed stage in the simulation and the statistical results are accurate.

E. Power extraction of the wind turbines

The power extracted by the wind turbines can be calculated directly based on the turbine induced force and wind velocity. Following Ref. 11, the total thrust force induced by a wind turbine can be written as

$$F_t = -\frac{1}{2}\rho\frac{C_T}{(1-a)^2}\langle u^T \rangle_d^2 \frac{\pi}{4}D^2. \quad (43)$$

The power extracted by an individual wind turbine is then obtained as

$$P_{ij}^* = -\left(\frac{1}{\rho}F_t\langle u^T \rangle_d\right)_{ij} = \left(\frac{1}{2}\frac{C_T}{(1-a)^2}\frac{\pi}{4}D^2\langle u^T \rangle_d^3\right)_{ij}, \quad (44)$$

where the subscript “ ij ” denotes the turbine at the i th row and j th column. The corresponding extracted power density by the turbine is defined as¹¹

$$\mathcal{P}_{ij} = \frac{P_{ij}^*}{s_x s_y D^2}. \quad (45)$$

In order to quantify the overall performance of the wind farm, we calculate the averaged value over the wind farm:

$$P_{\text{turbine}}^* = \frac{1}{N_{\text{row}}N_{\text{col}}}\sum_{i=1}^{N_{\text{row}}}\sum_{j=1}^{N_{\text{col}}}P_{ij}^*, \quad (46)$$

$$\mathcal{P}_T = \frac{1}{N_{\text{row}}N_{\text{col}}}\sum_{i=1}^{N_{\text{row}}}\sum_{j=1}^{N_{\text{col}}}\mathcal{P}_{ij}. \quad (47)$$

For the extracted power density, we also calculate its root-mean-square variation among different rows and columns as

$$\sigma_{\text{row}} = \sqrt{\frac{1}{N_{\text{row}}} \sum_{i=1}^{N_{\text{row}}} \left(\mathcal{P}_T - \frac{1}{N_{\text{col}}} \sum_{j=1}^{N_{\text{col}}} \mathcal{P}_{ij} \right)^2}, \quad (48)$$

$$\sigma_{\text{col}} = \sqrt{\frac{1}{N_{\text{col}}} \sum_{j=1}^{N_{\text{col}}} \left(\mathcal{P}_T - \frac{1}{N_{\text{row}}} \sum_{i=1}^{N_{\text{row}}} \mathcal{P}_{ij} \right)^2}. \quad (49)$$

As illustrated in Figs. 4 and 7, there exists large spatial variation for the instantaneous wind field around different wind turbines, caused by the complex interactions among the turbines within the turbine array as well as their interaction with the atmospheric boundary layer. Consequently, the extracted power densities \mathcal{P}_{ij} by different turbines exhibit appreciable variation, as shown in Fig. 15. Particularly, the variation of \mathcal{P}_{ij} among turbines in different columns is significant in both long and short terms [Fig. 15(a)]; the variation of \mathcal{P}_{ij} among turbines in different rows is mainly in short term, and the long term variation is relatively small [Fig. 15(b)]. The relatively larger among-column variation is clearly shown by the time-averaged values of σ_{row} and σ_{col} in Table VI. On the other hand, the averaged performance of the entire wind farm has much less temporal variation than those of the individual turbines, which is also shown in Fig. 15.

The frequency spectrum (denoted as E_F) of the turbine thrust force F_t can be calculated based on its time series, which is useful for the estimation of turbulence-induced fatigue load to the wind turbine. As an example, the spectrum E_F for case PM3 is shown in Fig. 16. Because the wave-correlated disturbance in the wind velocity field decays exponentially with height,^{20,41,63} no clear wave-correlated peak of E_F is observed at angular frequency $\omega \geq \omega_p$, where ω_p is the angular frequency at the wave spectrum peak [Table I]. The results for all the other cases are similar to case PM3 in Fig. 16, and are thus not shown here. We remark that if strong swells are present in the wave

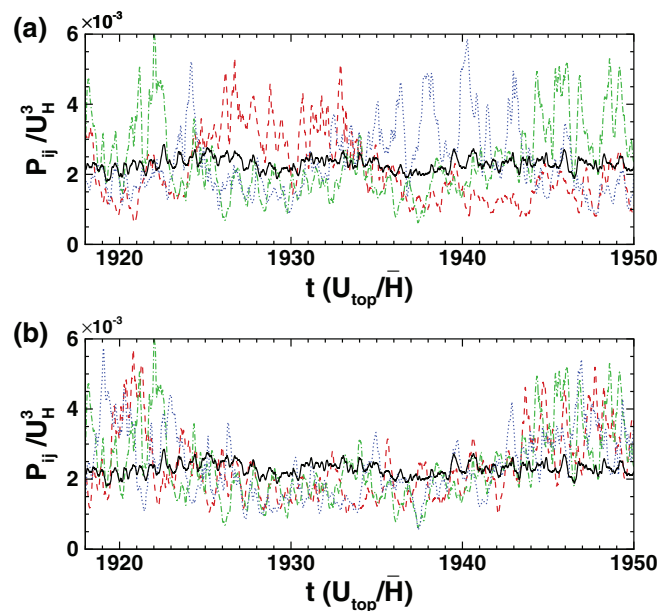


FIG. 15. Extracted wind power density for wind turbines at different columns (c) and rows (r) for case J3. In (a), the three wind turbines in the second row are shown: red dashed line, ($c1, r2$); green dashed-dotted line, ($c2, r2$); and blue dotted line, ($c3, r2$). In (b), the three wind turbines in the second column are shown: red dashed line, ($c2, r1$); green dashed-dotted line, ($c2, r2$); and blue dotted line, ($c2, r3$). The averaged value over the entire wind farm is indicated by black solid line.

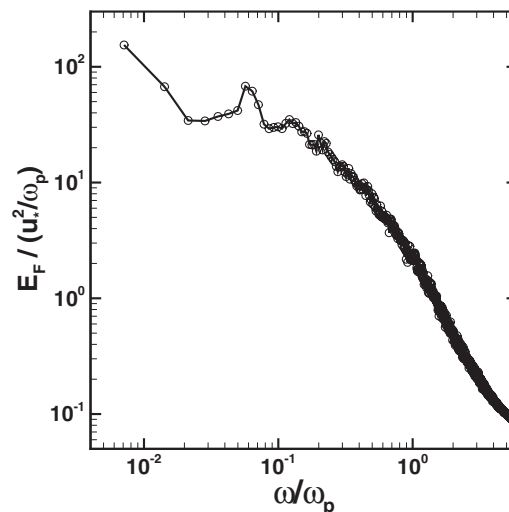
TABLE VI. Statistics of extracted power for various offshore wind farm cases. All of the values shown are after time averaging.

| Case | $\mathcal{P}_T/U_{\text{top}}^3$ | $P_{\text{turbine}}^*/(\rho D^2 U_{\text{top}}^3)$ | $\sigma_{\text{row}}/U_{\text{top}}^3$ | $\sigma_{\text{row}}/\mathcal{P}_T$ | $\sigma_{\text{col}}/U_{\text{top}}^3$ | $\sigma_{\text{col}}/\mathcal{P}_T$ |
|------|----------------------------------|--|--|-------------------------------------|--|-------------------------------------|
| J2 | 1.59×10^{-3} | 8.33×10^{-2} | 1.44×10^{-4} | 0.09 | 2.45×10^{-4} | 0.15 |
| J3 | 2.22×10^{-3} | 7.79×10^{-2} | 3.04×10^{-4} | 0.14 | 4.97×10^{-4} | 0.22 |
| J4 | 2.45×10^{-3} | 6.42×10^{-2} | 4.17×10^{-4} | 0.17 | 5.62×10^{-4} | 0.23 |
| PM2 | 1.64×10^{-3} | 8.63×10^{-2} | 1.44×10^{-4} | 0.09 | 2.91×10^{-4} | 0.18 |
| PM3 | 2.41×10^{-3} | 8.45×10^{-2} | 3.00×10^{-4} | 0.12 | 5.29×10^{-4} | 0.22 |
| PM4 | 2.48×10^{-3} | 6.50×10^{-2} | 4.45×10^{-4} | 0.18 | 5.43×10^{-4} | 0.22 |

field, their well organized long-crest long-wavelength form and fast propagation speed can induce strong variation in wind speed, leading to non-negligible wave-correlated contribution to E_F .

The time-averaged values of various statistical quantities for the extracted wind power are listed in Table VI. For a given turbine spacing, a wind farm above P–M waves extracts more power than that above JONSWAP waves does. As discussed in Secs. IV C and IV D, this increase of wind farm performance is caused by the stronger wave motion in the P–M wave cases compared with the JONSWAP wave cases. In the wake region behind each wind turbine, the deficit of wind speed causes the waves to feed momentum back to the wind. As shown in Table I, under the same wind forcing, the fully developed wave field (described by P–M spectrum) has larger peak wave phase speed than the fetch-limited wave field (described by JONSWAP spectrum) does. As a result, within the turbine wake regions, the P–M waves have relatively stronger capability to help recover the wind speed; out of the wake regions, the wind field experiences less wave resistance in the P–M wave cases than in the corresponding JONSWAP wave cases, resulting in slightly larger wind velocity near the wave surface as well as at the turbine rotor height. The turbines above the P–M waves thus have larger incident wind energy and achieve higher performance than the turbines above the JONSWAP waves.

For a dense wind turbine layout ($s_x = 5.25$), the streamwise distance between turbines is too small so that the waves in neither the P–M nor the JONSWAP cases have sufficient time to help recover the wind speed deficit in the turbine wake regions. This results in only 1.2% difference between cases J4 and PM4. One would imagine that for even lower values of s_x (not simulated in this study), the difference between JONSWAP and P–M cases is expected to be smaller. An extreme case would be that the turbines are deployed next to each other to form a turbine “forest.” Then the

FIG. 16. Frequency spectrum of the thrust force F_t for case PM3.

wind flow is affected mainly by the intensive interaction between the wind and the turbine forest, and the atmospheric flow cannot effectively feel the difference in wave condition. On the other hand, for a coarse wind turbine layout ($s_x = 10.5$), the wave-induced difference in \mathcal{P}_T is obvious, with case PM2 being 3.1% larger than case J2 due to the faster wind.

More importantly, for the intermediate streamwise turbine spacing $s_x = 7$ (commonly used in commercial wind farms), the velocity deficit in the turbine wake is larger than that for $s_x = 10.5$, resulting in stronger feedback from waves to wind. Meanwhile, the streamwise spacing of $s_x = 7$ is large enough so that waves have sufficient time to help recover the wind velocity in the turbine wake. The combined effects of the relatively faster wind at turbine height and the sufficient wave-enhanced recovery of wind velocity in the wake region result in a prominent difference of 8.6% between cases PM3 and J3. It should be remarked that, in this study only a relatively large fetch of 80.0 km is considered, which corresponds to a peak wavelength of 60 m. In the oceans, fetch value varying from $O(1)$ km to $O(100)$ km can result in a variation of $O(1)$ – $O(100)$ m for the peak wavelength and $O(1)$ – $O(10)$ m/s for the peak wave phase speed. Therefore, the wave-induced effect on the wind farm performance can be even larger than the 8.6% difference found in this study, depending on the environmental wind and wave conditions. This suggests that the sea-surface wave effect should be an important factor in planning offshore wind farms.

V. CONCLUSIONS

With larger available space, faster winds, and relatively less visual impact and noise, offshore wind power has become a new research frontier. Offshore wind farms operate in a complex environment. The sea surface is covered by progressive surface waves of various sizes that interact with the wind over a wide range of scales. Thus a deep understanding of the offshore wind farm dynamics and an accurate prediction of wind farm performance require consideration of turbine–wind–wave coupling dynamics.

In this study, a hybrid numerical capability has been developed for the simulation of large scale offshore wind farms. The numerical framework consists of: (i) a large-eddy simulation of wind turbulence on a curvilinear coordinate system that follows the wave motion; (ii) a spectral simulation of nonlinear sea-surface waves with high resolution; and (iii) an actuator-disk model for the wind turbines. These modeling tools are coupled in the simulation for the first time to capture the complex flow physics of offshore wind farms. The current numerical method has been tested for the simulation of wind past both a single wind turbine and a very large wind farm. Validation is done by comparing the current simulation results with experimental and numerical results reported in the literature.

In our simulation, a very large wind farm is modeled with “infinite” turbine array (by means of periodic boundary conditions in the horizontal directions). The turbine array boundary layer is considered to be fully developed. The sea surface is covered by a wind-generated wave field, with both fetch-limited condition (described by JONSWAP spectrum) and fully developed condition (described by P–M spectrum) being considered. For the wind farm configuration, various streamwise spacings (i.e., $s_x = 10.5, 7$, and 5.25) are investigated. Based on the simulation data, the characteristics of offshore wind turbine array boundary layers are studied, with a focus on time- and horizontal-averaged statistics.

In particular, compared with those under the fetch-limited condition, the waves under the fully developed condition are relatively faster, and thus exert less resistance to the wind. This difference results in smaller friction velocity below the turbine layer (u_{*10}), smaller effective sea-surface roughness ($z_{0,10}$), and smaller effective roughness of wind farm to the atmosphere above it ($z_{0,hi}$). Therefore, the wind field in the turbine layer is relatively stronger in the P–M wave cases than in the JONSWAP cases. Analysis of the mean kinetic energy budget shows that, for the fully developed wave condition, larger vertical flux enters the turbine layer from above to lead to more turbine work. This result is also confirmed by the direct calculation of power extraction by the wind turbines.

Change of streamwise turbine spacing leads to different offshore wind farm statistics. A decrease of streamwise spacing results in an increase of turbine density in the wind farm, and causes a decrease

of u_{*lo} and an increase of $z_{0,hi}$. For the wind farm performance, the simulation result shows that when the turbine spacing is reduced, the extracted power density increases while the extracted power per wind turbine decreases. With the ratio of “cost per area/cost per turbine” known in the future, the optimal turbine spacing for a particular offshore wind farm may be determined in follow-up work.

In this study, wind-induced waves are found to have appreciable effect on wind farm performance. Previous analysis on offshore wind farm often neglected the wind-seas effect based on the assumption that the direct distortion by the waves on the wind decays exponentially with height and thus becomes negligible at turbine rotor height. However, the waves affect the wind field in many ways, such as the sea-surface roughness and the vertical transport of momentum and kinetic energy as discussed in this paper. For a streamwise turbine spacing of $s_x = 7$ commonly used in commercial wind farms, our LES result shows a prominent 8.3% increase of wind power extraction rate for the P–M wave case compared with the corresponding JONSWAP wave case due to the relatively stronger motions of the P–M waves. Note that a fetch value of 80 km is considered in this study for the JONSWAP waves. In the oceans, the fetch can have a wide range of values, some are smaller so that the peak waves are shorter and slower compared with the present simulation case. (Cases with shorter fetches are not simulated in this study due to the increased requirement on grid resolution as the peak waves become shorter.) These shorter fetch JONSWAP cases are expected to have even bigger difference from the P–M case. Finally, we remark that if swells are present at the offshore wind farm site, the wave effect is expected to be even more significant due to the long wavelength and fast propagation speed of the swells. The swells also induce strong periodic distortion to the wind field, which may lead to periodic fluctuations in the power output of the wind turbines. Effect of swells on the offshore wind farm will be a subject of our research of next step and the results will be reported in the future.

ACKNOWLEDGMENTS

D.Y. and L.S. acknowledge the support of NSF-CBET-1341062 on the wind energy study and the support of ONR on some of the development of the wind–wave simulation tool. C.M. acknowledges the support of NSF-AGS-1045189 and NSF-OISE-1243482.

APPENDIX A: NUMERICAL DETAILS OF HIGH-ORDER SPECTRAL METHOD

A major feature of the Zakharov formulation is that the kinematic and dynamic conditions are satisfied at the true wave surface. In order to take advantage of this feature, the HOSM uses a perturbation series of Φ with respect to wave steepness to order M and the Taylor series expansion about the mean water level $z = 0$ to the corresponding order,

$$\Phi(x, y, z, t) = \sum_{m=1}^M \Phi^{(m)}(x, y, z, t), \quad (\text{A1})$$

$$\Phi^s(x, y, t) = \sum_{m=1}^M \sum_{\ell=0}^{M-m} \frac{\eta^\ell}{\ell!} \frac{\partial^\ell}{\partial z^\ell} \Phi^{(m)}(x, y, z, t) \Big|_{z=0}. \quad (\text{A2})$$

The perturbation mode $\Phi^{(m)}$ is further decomposed using an eigenfunction expansion with N modes,

$$\Phi^{(m)}(x, y, z, t) = \sum_{k=1}^N \Phi_k^{(m)}(t) \Psi_k(x, y, z). \quad (\text{A3})$$

In this study, we consider the deep water condition only, for which the eigenfunctions Ψ_k are

$$\Psi_k(x, y, z) = \exp(|\mathbf{k}|z + i\mathbf{k} \cdot \mathbf{x}). \quad (\text{A4})$$

Here $i = \sqrt{-1}$; and $\mathbf{k} = (k_x, k_y)$ is the wavenumber vector, which is related to the scalar wavenumber k through $k = |\mathbf{k}| = \sqrt{k_x^2 + k_y^2}$. We remark that the HOSM can be further generalized by replacing

the eigenfunctions Ψ_k in Eq. (A4) with other more complex functions that account for finite and vary water depth.^{38,64–66}

Note that the eigenfunctions in Eq. (A4) ensure that the resultant velocity potential Φ satisfies the incompressibility constraint, Eq. (15). Substitution of Eqs. (A1)–(A4) into Eqs. (13) and (14) results in the evolution equations for η and Φ^s .³⁸

$$\frac{\partial \eta}{\partial t} = -\nabla_h \eta \cdot \nabla_h \Phi^s + (1 + \nabla_h \eta \cdot \nabla_h \eta) \times \left[\sum_{m=1}^M \sum_{\ell=0}^{M-m} \frac{\eta^\ell}{\ell!} \sum_{k=1}^N \Phi_k^{(m)}(t) \frac{\partial^{\ell+1} \Psi_k(x, y, z)}{\partial z^{\ell+1}} \Big|_{z=0} \right], \quad (\text{A5})$$

$$\frac{\partial \Phi^s}{\partial t} = -g\eta - \frac{1}{2} \nabla_h \Phi^s \cdot \nabla_h \Phi^s - \frac{p_a(x, y, t)}{\rho_w} + \frac{1}{2} (1 + \nabla_h \eta \cdot \nabla_h \eta) \times \left[\sum_{m=1}^M \sum_{\ell=0}^{M-m} \frac{\eta^\ell}{\ell!} \sum_{k=1}^N \Phi_k^{(m)}(t) \frac{\partial^{\ell+1} \Psi_k(x, y, z)}{\partial z^{\ell+1}} \Big|_{z=0} \right]^2. \quad (\text{A6})$$

In HOSM, Eqs. (A5) and (A6) are advanced in time by a fourth-order Runge–Kutta scheme. The equations are discretized in space by a Fourier-series-based pseudo-spectral method. The quadratic terms are de-aliased with the 3/2 rule. The HOSM has an exponential convergence rate of the solution with respect to M and N , and requires a computational cost proportional to $MM \ln N$ only. It has been applied to a wide range of nonlinear wave problems, e.g., instability of steep Stokes waves,³⁸ generation of ship waves by moving surface disturbance,⁶⁷ and prediction of rogue wave occurrence.⁵⁶ A complete review of the methodology, validation, and application of the HOSM is provided in Chap. 15 of Ref. 54.

APPENDIX B: SPECTRAL DESCRIPTION OF WIND-GENERATED SEA-SURFACE WAVES

For the fully developed sea condition, the sea-surface wave elevation satisfies the P–M spectrum.³² In the frequency domain, the P–M spectrum is described by

$$E_{\text{pm}}(\omega) = \frac{\alpha_{\text{pm}} g^2}{\omega^5} \exp \left[-1.69 \beta_{\text{pm}} \left(\frac{\omega_p}{\omega} \right)^4 \right]. \quad (\text{B1})$$

Here, $\alpha_{\text{pm}} = 8.1 \times 10^{-3}$; $\beta_{\text{pm}} = 0.74$; ω is the angular frequency; $\omega_p = 0.877 g/U_{19.5}$ is the frequency of the spectrum peak; and $U_{19.5}$ is the wind speed at a height of 19.5 m above the sea surface. The values of these parameters were obtained by Pierson and Moskowitz³² using the measurement data from British weather ships in the north Atlantic. The 19.5 m reference height is the height of the anemometers on the weather ships. Based on the dispersion relation for deep water waves, $\omega^2 = gk$, Eq. (B1) is transformed to Eq. (21) in wavenumber space using

$$S_{\text{pm}}(k) = \frac{g}{2\omega} E_{\text{pm}}(\omega). \quad (\text{B2})$$

For the developing sea condition, a widely used wave spectrum is the JONSWAP spectrum obtained during the Joint North Sea Wave Project.³¹ Its frequency-domain spectral form is expressed as

$$E_J(\omega) = \frac{\alpha_J g^2}{\omega^5} \exp \left[-\frac{5}{4} \left(\frac{\omega_p}{\omega} \right)^4 \right] \gamma^r, \quad (\text{B3})$$

where

$$r = \exp \left[-\frac{(\omega - \omega_p)^2}{2\sigma^2 \omega_p^2} \right], \quad (\text{B4})$$

$$\alpha_J = 0.076 \left(\frac{U_{10}^2}{gF} \right)^{0.22}, \quad (\text{B5})$$

$$\omega_p = 22 \left(\frac{g^2}{U_{10} F} \right)^{1/3}, \quad (\text{B6})$$

$$\gamma = 3.3, \quad (\text{B7})$$

$$\sigma = \begin{cases} 0.07 & \omega \leq \omega_p, \\ 0.09 & \omega > \omega_p. \end{cases} \quad (\text{B8})$$

Here, F , called the fetch, is the distance over which the wind has been blowing; γ is the peak enhancement factor; and U_{10} is the wind speed at a height of 10 m above the sea surface. Equation (B3) is transferred to Eq. (20) in the wavenumber domain also through the dispersion relation (B2).

- ¹H. Snel, "Review of the present status of rotor aerodynamics," *Wind Energy* **1**, 46 (1998).
- ²A. Crespo, J. Hernández, and S. Frandsen, "Survey of modeling methods for wind turbine wakes and wind farms," *Wind Energy* **2**, 1 (1999).
- ³T. Burton, D. Sharpe, N. Jenkins, and E. Bossanyi, *Wind Energy Handbook* (Wiley, 2001).
- ⁴L. J. Vermeer, J. N. Sørensen, and A. Crespo, "Wind turbine wake aerodynamics," *Prog. Aeronaut. Sci.* **39**, 467 (2003).
- ⁵A. Jimenez, A. Crespo, E. Migoya, and J. Garcia, "Advances in large-eddy simulation of a wind turbine wake," *J. Phys.: Conf. Ser.* **75**, 012041 (2007).
- ⁶A. Jimenez, A. Crespo, E. Migoya, and J. Garcia, "Large-eddy simulation of spectral coherence in a wind turbine wake," *Environ. Res. Lett.* **3**, 015004 (2008).
- ⁷N. Troldborg, J. N. Sorensen, and R. Mikkelsen, "Numerical simulations of wake characteristics of a wind turbine in uniform inflow," *Wind Energy* **13**, 86 (2010).
- ⁸Y.-T. Wu and F. Porté-Agel, "Large-eddy simulation of wind-turbine wakes: evaluation of turbine parametrisations," *Boundary-Layer Meteorol.* **138**, 345 (2011).
- ⁹L. P. Chamorro and F. Porté-Agel, "Effects of thermal stability and incoming boundary-layer flow characteristics on wind-turbine wakes: a wind-tunnel study," *Boundary-Layer Meteorol.* **136**, 515 (2010).
- ¹⁰S. Baidya Roy, S. W. Pacala, and R. L. Walko, "Can large wind farms affect local meteorology?" *J. Geophys. Res.* **109**, D19101, doi:10.1029/2004JD004763 (2004).
- ¹¹M. Calaf, C. Meneveau, and J. Meyers, "Large eddy simulation study of fully developed wind-turbine array boundary layers," *Phys. Fluids* **22**, 015110 (2010).
- ¹²E. Hau, *Wind Turbines: Fundamentals, Technologies, Applications, Economics* (Springer, Berlin, 2005).
- ¹³R. B. Cal, J. Lebrón, L. Castillo, H. S. Kang, and C. Meneveau, "Experimental study of the horizontally averaged flow structure in a model wind-turbine array boundary layer," *J. Renewable Sustainable Energy* **2**, 013106 (2010).
- ¹⁴X. Yang, S. Kang, and F. Sotiropoulos, "Computational study and modeling of turbine spacing effects in infinite aligned wind farms," *Phys. Fluids* **24**, 115107 (2012).
- ¹⁵L. P. Chamorro and F. Porté-Agel, "Turbulent flow inside and above a wind farm: a wind-tunnel study," *Energies* **4**, 1916 (2011).
- ¹⁶S. Butterfield, W. Musial, J. Jonkman, and P. D. Sclavounos, "Engineering challenges for floating offshore wind turbines," National Renewable Energy Laboratory, Technical Report No. NREL/CP-500-38776, 2007.
- ¹⁷U.S. Department of Energy, "20% wind energy by 2030: Increasing wind energy's contribution to U.S. electricity supply," Technical Report No. DOE/GO-102008-2567, 2008.
- ¹⁸P. P. Sullivan and J. C. McWilliams, "Dynamics of winds and currents coupled to surface waves," *Annu. Rev. Fluid Mech.* **42**, 19 (2010).
- ¹⁹R. L. Snyder, F. W. Dobson, J. A. Elliott, and R. B. Long, "Array measurements of atmospheric pressure fluctuations above surface gravity waves," *J. Fluid Mech.* **102**, 1 (1981).
- ²⁰M. A. Donelan, A. V. Babanin, I. R. Young, and M. L. Banner, "Wave-follower field measurements of the wind-input spectral function," *J. Phys. Oceanogr.* **36**, 1672 (2006).
- ²¹D. S. Henn and R. I. Sykes, "Large-eddy simulation of flow over wavy surfaces," *J. Fluid Mech.* **383**, 75 (1999).
- ²²V. Armenio and U. Piomelli, "A Lagrangian mixed subgrid-scale model in generalized coordinates," *Flow, Turbul. Combust.* **65**, 51 (2000).
- ²³P. P. Sullivan, J. E. Edson, T. Hristov, and J. C. McWilliams, "Large-eddy simulations and observations of atmospheric marine boundary layers above nonequilibrium surface waves," *J. Atmos. Sci.* **65**, 1225 (2008).
- ²⁴D. Yang and L. Shen, "Simulation of viscous flows with undulatory boundaries. Part I: Basic solver," *J. Comput. Phys.* **230**, 5488 (2011).
- ²⁵D. Yang and L. Shen, "Simulation of viscous flows with undulatory boundaries. Part II: Coupling with other solvers for two-fluid computations," *J. Comput. Phys.* **230**, 5510 (2011).
- ²⁶Y. Liu, D. Yang, X. Guo, and L. Shen, "Numerical study of pressure forcing of wind on dynamically evolving water waves," *Phys. Fluids* **22**, 041704 (2010).
- ²⁷J. Meyers and C. Meneveau, "Optimal turbine spacing in fully developed wind farm boundary layers," *Wind Energy* **15**, 305 (2012).
- ²⁸E. Bou-Zeid, C. Meneveau, and M. Parlange, "A scale-dependent lagrangian dynamic model for large eddy simulation of complex turbulent flows," *Phys. Fluids* **17**, 025105 (2005).

- ²⁹ E. N. Wayman, P. D. Sclavounos, S. Butterfield, J. Jonkman, and W. Musial, "Coupled dynamic modeling of floating wind turbine systems," National Renewable Energy Laboratory, Technical Report No. NREL/CP-500-39481, 2006.
- ³⁰ D. Roddier, C. Cermelli, A. Aubault, and A. Weinstein, "WindFloat: A floating foundation for offshore wind turbines," *J. Renewable Sustainable Energy* **2**, 033104 (2010).
- ³¹ K. Hasselmann, T. P. Barnett, E. Bouws, H. Carlson, D. E. Cartwright, K. Enke, J. A. Ewing, H. Gienapp, D. E. Hasselmann, P. Kruseman, A. Meerburg, P. Müller, D. J. Olbers, K. Richter, W. Sell, and H. Walden, "Measurements of wind-wave growth and swell decay during the Joint North Sea Wave Project (JONSWAP)," *Dtsch. Hydrogr. Z. Suppl.* **8**, N12 (1973).
- ³² W. J. Pierson and L. Moskowitz, "A proposed spectral form for fully developed wind seas based on the similarity theory of S. A. Kitaigorodskii," *J. Geophys. Res.* **69**, 5181, doi:10.1029/JZ069i024p05181 (1964).
- ³³ J. Meyers and C. Meneveau, "Large eddy simulation of large wind-turbine arrays in the atmospheric boundary layer," AIAA Paper 2010-827, 2010.
- ³⁴ M. Calaf, M. Parlange, and C. Meneveau, "Large eddy simulation study of scalar transport in fully developed windturbine array boundary layers," *Phys. Fluids* **23**, 126603 (2011).
- ³⁵ C. Meneveau, T. Lund, and W. Cabot, "A Lagrangian dynamic subgrid-scale model of turbulence," *J. Fluid Mech.* **319**, 353 (1996).
- ³⁶ F. Porté-Agel, C. Meneveau, and M. B. Parlange, "A scale-dependent dynamic model for large-eddy simulation: application to a neutral atmospheric boundary layer," *J. Fluid Mech.* **415**, 261 (2000).
- ³⁷ F. Wan, F. Porté-Agel, and R. Stoll, "Evaluation of dynamic subgrid-scale models in large-eddy simulations of neutral turbulent flow over a two-dimensional sinusoidal hill," *Atmos. Environ.* **41**, 2719 (2007).
- ³⁸ D. G. Dommermuth and D. K. P. Yue, "A high-order spectral method for the study of nonlinear gravity waves," *J. Fluid Mech.* **184**, 267 (1987).
- ³⁹ V. E. Zakharov, "Stability of periodic wave of finite amplitude on the surface of a deep fluid," *J. Appl. Mech. Tech. Phys.* **9**, 190 (1968).
- ⁴⁰ D. Yang and L. Shen, "Characteristics of coherent vortical structures in turbulent flows over progressive surface waves," *Phys. Fluids* **21**, 125106 (2009).
- ⁴¹ D. Yang and L. Shen, "Direct-simulation-based study of turbulent flow over various waving boundaries," *J. Fluid Mech.* **650**, 131 (2010).
- ⁴² J. N. Sørensen and W. Z. Shen, "Numerical modeling of wind turbine wakes," *J. Fluids Eng.* **124**, 393 (2002).
- ⁴³ L. Ge and F. Sotiropoulos, "A numerical method for solving the 3D unsteady incompressible Navier–Stokes equations in curvilinear domains with complex immersed boundaries," *J. Comput. Phys.* **225**, 1782 (2007).
- ⁴⁴ F. Porté-Agel, Y.-T. Wu, H. Lu, and R. J. Conzemius, "Large-eddy simulation of atmospheric boundary layer flow through wind turbines and wind farms," *J. Wind Eng. Ind. Aerodyn.* **99**, 154 (2011).
- ⁴⁵ J. Smagorinsky, "General circulation experiments with the primitive equations. I. The basic experiment," *Mon. Weather Rev.* **91**, 99 (1963).
- ⁴⁶ R. J. A. M. Stevens, D. F. Gayme, and C. Meneveau, "Effect of turbine alignment on the average power output of wind-farms," in *Proceedings of the 2013 International Conference on Aerodynamics of Offshore Wind Energy Systems and Wakes* (Technical University of Denmark, 2013), p. 611; see <http://indico.conferences.dtu.dk/internalPage.py?pageId=13&confId=126>.
- ⁴⁷ C. VerHulst and C. Meneveau, "LES study of the impact of various wind turbine actuator forcings on kinetic energy entrainment in large wind farms," in *Proceedings of the 2013 International Conference on Aerodynamics of Offshore Wind Energy Systems and Wakes* (Technical University of Denmark, 2013), p. 657; See <http://indico.conferences.dtu.dk/internalPage.py?pageId=13&confId=126>.
- ⁴⁸ R. J. A. M. Stevens, J. Graham, and C. Meneveau, "A concurrent precursor inflow method for Large Eddy Simulations and applications to finite length wind farms," *Renewable Energy* (to be published).
- ⁴⁹ M. R. Raupach, R. A. Antonia, and S. Rajagopalan, "Rough-wall turbulent boundary layers," *Appl. Mech. Rev.* **44**, 1 (1991).
- ⁵⁰ O. Coceal, T. G. Thomas, I. P. Castro, and S. E. Belcher, "Mean flow and turbulence statistics over groups of urban-like cubical obstacles," *Boundary-Layer Meteorol.* **121**, 491 (2006).
- ⁵¹ S. E. Belcher and J. C. R. Hunt, "Turbulent flow over hills and waves," *Annu. Rev. Fluid Mech.* **30**, 507 (1998).
- ⁵² D. E. Hasselmann, M. Dunkel, and J. A. Ewing, "Directional wave spectra observed during JONSWAP 1973," *J. Phys. Oceanogr.* **10**, 1264 (1980).
- ⁵³ D. G. Dommermuth, "The initialization of nonlinear waves using an adjustment scheme," *Wave Motion* **32**, 307 (2000).
- ⁵⁴ C. C. Mei, M. Stiassnie, and D. K. P. Yue, *Theory and Applications of Ocean Surface Waves Part 2: Nonlinear Aspects* (World Scientific, Singapore, 2005).
- ⁵⁵ D. G. Dommermuth, T. C. Fu, K. A. Brucker, T. T. O'Shea, and D. C. Wyatt, "Numerical prediction of a seaway," in *Proceedings of the 28th Symposium on Naval Hydrodynamics* (Office of Naval Research, Arlington, VA, USA, 2010), p. 276.
- ⁵⁶ W. Xiao, Y. Liu, G. Wu, and D. K. P. Yue, "Rogue wave occurrence and dynamics by direct simulations of nonlinear wavefield evolution," *J. Fluid Mech.* **720**, 357 (2013).
- ⁵⁷ D. Yang, C. Meneveau, and L. Shen, "Dynamic modeling of sea-surface roughness for large-eddy simulation of wind over ocean wavefield," *J. Fluid Mech.* **726**, 62 (2013).
- ⁵⁸ H. Charnock, "Wind stress on a water surface," *Q. J. R. Meteorol. Soc.* **81**, 639 (1955).
- ⁵⁹ Y. Toba, S. D. Smith, and N. Ebuchi, "Historical drag expressions," in *Wind Stress Over the Ocean*, edited by I. S. F. Jones and Y. Toba (Cambridge University Press, New York, 2001), pp. 35–53.
- ⁶⁰ D. Yang, L. Shen, and C. Meneveau, "An assessment of dynamic subgrid-scale sea-surface roughness models," *Flow, Turbul. Combust.* **91**, 541 (2013).

- ⁶¹J. O'Neil and C. Meneveau, "Subgrid-scale stresses and their modelling in a turbulent plane wake," *J. Fluid Mech.* **349**, 253 (1997).
- ⁶²S. Frandsen, "On the wind speed reduction in the center of large clusters of wind turbines," *J. Wind Eng. Ind. Aerodyn.* **39**, 251 (1992).
- ⁶³P. P. Sullivan, J. C. McWilliams, and C.-H. Moeng, "Simulation of turbulent flow over idealized water waves," *J. Fluid Mech.* **404**, 47 (2000).
- ⁶⁴Y. Liu and D. K. P. Yue, "On generalized Bragg scattering of surface waves by bottom ripples," *J. Fluid Mech.* **356**, 297 (1998).
- ⁶⁵M.-R. Alam, Y. Liu, and D. K. P. Yue, "Oblique sub- and super-harmonic Bragg resonance of surface waves by bottom ripples," *J. Fluid Mech.* **643**, 437 (2010).
- ⁶⁶M.-R. Alam, Y. Liu, and D. K. P. Yue, "Attenuation of short surface waves by the sea floor via nonlinear sub-harmonic interaction," *J. Fluid Mech.* **689**, 529 (2011).
- ⁶⁷D. G. Dommermuth and D. K. P. Yue, "The nonlinear three-dimensional waves generated by a moving surface disturbance," in *Proceedings of the 17th Symposium on Naval Hydrodynamics, Hague, The Netherlands* (National Academy Press, Washington DC, 1988).